J. Fluid Mech. (1989), *vol.* 198, *pp.* 199–230
Printed in Great Britain

Statistical properties of decaying geostrophic turbulence

By JAMES C. McWILLIAMS

Geophysical Turbulence Program, National Center for Atmospheric Research,
Boulder, CO 80307, USA

(Received 4 December 1987 and in revised form 8 June 1988)

High-resolution, high-Reynolds-number numerical solutions of fully three-dimensional, decaying, geostrophic turbulence are examined. The results include the demonstration of a substantial degree of similarity between geostrophic and two-dimensional turbulence: transfer of energy to larger scales; transfer of potential enstrophy to smaller scales; vanishing energy dissipation as the Reynolds number increases; the emergence and growth to dominance of isolated, coherent vortices; and a competition between the vortices and Rossby waves, with an associated horizontal anisotropy when the latter are dominant. Properties that are distinct to geostrophic turbulence include the following: approximate three-dimensional wavenumber isotropy, with significant departures on large scales due to boundedness of the domain and on smaller scales due to anisotropic spectrum transfer rates; insensitivity of solution properties to anisotropy or vertical inhomogeneity in the dissipation; persistence of vertical inhomogeneity; development of inhomogeneity due to solid vertical boundaries; and the processes of alignment, attachment, and vertical straining associated with the finite vertical extent of the coherent vortices.

1. Introduction

Large-scale atmospheric and oceanic fluid motions are usually approximately geostrophic due to the influence of planetary rotation. An idealization of this regime is weakly dissipative flow in a stably stratified fluid in a rapidly rotating domain. A parametric specification is Reynolds number large, Rossby number ($R \equiv U/fL$) small, Richardson number ($Ri \equiv (NH/U)^2$) large, and Burger number ($B \equiv R^2 Ri$) not too small. (U is a characteristic horizontal velocity, H and L are vertical and horizontal lengths, f is a Coriolis frequency (rotation rate), and N is a Brunt–Väisälä frequency (stratification strength).) Advectively controlled flow with limited predictability in this regime is called geostrophic turbulence.

The principal antecedents of the present investigation of fully three-dimensional geostrophic turbulence are Charney (1971), Herring (1980), and Hua & Haidvogel (1986). Charney noted the formal analogy with two-dimensional turbulence, and, on the basis of the coordinate symmetries and inviscid conservation laws, he proposed the occurrence of inverse cascade of energy (transfer to larger scales), forward cascade (transfer to smaller scales) of potential enstrophy (volume-mean-square potential vorticity), three-dimensional isotropy (i.e. energy and enstrophy spectra independent of wavenumber direction, once the vertical coordinate has been rescaled by N/f), and the associated energy equipartition (potential energy equal to half the kinetic energy). Herring investigated these proposals in an initial-value problem for a statistical closure model, and generally confirmed them. Hua & Haidvogel drew similar conclusions from intermediate-resolution computational solutions for equilibrium geostrophic turbulence sustained by a mean flow with vertical shear. In addition, there have been many other investigations of the processes in geostrophic turbulence in models with low vertical resolution, typically one or two vertical degrees of freedom; these studies are discussed in review articles by Rhines (1979), Salmon (1982), McWilliams (1983), and Holloway (1986).

The present study is of initial-value problems with slowly decaying energy (large Reynolds number), based upon computational solutions of unprecedentedly high resolution, in all three spatial dimensions. The principal issues, partly inherited from the antecedent studies, are the following:

(i) the dynamical similarities between two-dimensional and geostrophic turbulence;
(ii) spectrum transfers of energy and potential enstrophy;
(iii) three-dimensional isotropy and equipartition;
(iv) vertical inhomogeneity;
(v) vertical boundary effects;
(vi) anisotropic and vertically inhomogeneous dissipation;
(vii) coexistence of turbulence and Rossby waves (supported by a spatial gradient in f);
(viii) the emergence of and eventual dominance of the flow by isolated, coherent vortices.

The latter has been shown to occur in two-dimensional turbulence (McWilliams 1984; Herring & McWilliams 1985; Benzi, Patarnello & Santangelo 1988), and a principal result of this study is that it occurs in geostrophic turbulence as well.

2. Posing the problem

The governing quasi-geostrophic equations are asymptotically valid as $R \rightarrow 0$. After non-dimensionalization by H, L, U, N, and f scales (in particular, the timescale is L/U), the potential vorticity equation is

$$\frac{\partial q}{\partial t} + \mathrm{J}\left(\psi, q + \frac{f}{R}\right) = \mathscr{F}, \tag{1}$$

where the potential vorticity is defined by

$$q = \zeta + \eta, \tag{2}$$

with components

$$\zeta = \left(\frac{\partial^2}{\partial x^2} + \frac{\partial^2}{\partial y^2}\right)\psi, \quad \eta = \frac{\partial}{\partial z}\left(\frac{1}{N^2(z)}\frac{\partial}{\partial z}\right)\psi. \tag{3}$$

Respectively, these are the vertical component of vorticity and the contribution from vortex stretching in the vertical. The vertical direction is parallel to the axis of rotation and the acceleration of gravity. The Coriolis frequency is

$$f = 1 + R\beta(y - \pi), \tag{4}$$

where β represents its spatial gradient (note that $\mathrm{J}(\psi, f/R) = \beta\,\partial\psi/\partial x$ is $O(1)$ as $R \rightarrow 0$). ψ is the stream function, and it is related to the horizontal velocity components by

$$u = -\frac{\partial\psi}{\partial y}, \quad v = \frac{\partial\psi}{\partial x}. \tag{5}$$

The operator J in (1) is the horizontal Jacobian, and it represents horizontal advection. $N(z)$ is the non-dimensional Brunt–Väisälä frequency (i.e. the vertical gradient of the mean density profile).

t is the temporal coordinate. The horizontal coordinates are x and y, their range is $[0, 2\pi]$, and the lateral boundary condition is periodicity. The vertical coordinate is z, its range is $[0, \pi]$, and the vertical boundaries are rigid, uniform-density surfaces, viz.

$$\frac{\partial \psi}{\partial z} = 0 \quad \text{at} \quad z = 0, \pi. \tag{6}$$

An alternative choice of a vertical boundary condition of periodicity would be analogous to the horizontal one and would be somewhat more conducive than (6) to three-dimensional isotropy and vertical homogeneity. However, the rigid-lid condition is preferred because it is more geophysically relevant (the ocean and atmosphere are vertically bounded on scales comparable with their most energetic flows), because significant departures from three-dimensional isotropy and homogeneity occur even with periodicity (see §§5 and 9 below), and because twice as many vertical modes are required to span a given range of vertical wavenumbers with a periodicity condition, which is therefore computationally more expensive than a rigid-surface condition.

When $\mathscr{F} = 0$, two quadratic invariants are the total energy and potential enstrophy,

$$T = \frac{1}{2}\left\{u^2+v^2+\frac{1}{N^2}\left(\frac{\partial \psi}{\partial z}\right)^2\right\}, \quad V = \tfrac{1}{2}\{q^2\}, \tag{7}$$

where $\{\cdot\}$ denotes a volume average. More generally, the non-conservative torque is defined by

$$\mathscr{F} = -\nu_{\mathrm{h}}\left(\frac{\partial^2}{\partial x^2}+\frac{\partial^2}{\partial y^2}\right)^2 \zeta - \nu_{\mathrm{v}}\frac{\partial^4}{\partial z^4}\zeta - \epsilon\zeta\delta(z). \tag{8}$$

The model is thus an adiabatic one in that it is non-conservative only in momentum but not in density. (An adiabatic, quasi-geostrophic, rigid-lid model is ill posed with non-uniform boundary densities – i.e. $\partial\psi/\partial z \neq 0$ at $z = 0$ and π – which would evolve as a passive tracer and thus cascade to arbitrarily small horizontal scales without buoyancy dissipation.) The first two terms on the right-hand side of (8) are fourth-order frictions in the horizontal and vertical, respectively. This is a subgrid-scale closure model which acts locally in both physical and wavenumber space, and which is more concentrated on smaller scales in its effects than is the second-order Newtonian viscosity of the Navier–Stokes equations. This closure model is inherently *ad hoc*, but considerable experience with it in oceanic and atmospheric models has shown that, compared to Newtonian viscosity: the benefit of less damped large-scale flows is achieved without introducing significant spurious effects, this property is illustrated for two-dimensional turbulence in McWilliams (1984). Since these terms are of higher differential order, additional boundary conditions are required. In the horizontal, periodicity suffices at all orders. In the vertical, the choice of (6) plus

$$\frac{\partial \zeta}{\partial z} = \frac{\partial^3 \zeta}{\partial z^3} = 0 \quad \text{at} \quad z = 0, \pi, \tag{9}$$

when $\nu_{\mathrm{v}} \neq 0$, yields negative definite viscous dissipation terms in the budgets for T and for kinetic enstrophy, $\{\zeta^2\}$. In the V-budget, however, the ν_{h} terms are always negative definite, whereas the ν_{v} terms are so only if $N(z)$ is a constant. The final term in (8) is a bottom frictional torque due to an Ekman boundary layer (note that in both the atmosphere and the ocean, the lower boundary supports stress but the upper one does not). This torque yields negative definite dissipation for T and $\{\zeta^2\}$, but not V.

When $N(z)$ is a constant, q in (2)–(3) is the three-dimensional Laplacian of ψ when the vertical coordinate is rescaled to be zN. In both T and V, rescaled vertical derivatives of ψ enter symmetrically with horizontal ones. This is the basis for Charney's (1971) hypothesis that $\psi(x,y,z)$ be three-dimensional isotropic in its dependence upon the spatial coordinates. Note that this is quite different from velocity isotropy: in the quasi-geostrophic equations, the vertical velocity is small (i.e. $O(R)$) compared with the horizontal velocity.

3. Computations

The quasi-geostrophic equations are solved numerically in a pseudospectral Galerkin model. The solution is represented as

$$\psi(\boldsymbol{x},z,t) = \sum_{\boldsymbol{k}} \sum_{p} \hat{\psi}_p(\boldsymbol{k},t)\, \mathrm{e}^{\mathrm{i}\boldsymbol{k}\cdot\boldsymbol{x}}\, F_p(z), \tag{10}$$

where p is a vertical mode index ($0 \leqslant p \leqslant N_z - 1$), $\boldsymbol{x} = (x,y)$, and $\boldsymbol{k}$ is a horizontal wavenumber vector, whose components have integer values and are selected by approximately circular truncation consistent with horizontal dealiassing of J and conservation of T and V when $\mathscr{F} = 0$ (neglecting time-stepping errors). This computational technique is a three-dimensional generalization of the method of Orszag (1971), and the treatment of the vertical modes is discussed in Hua & Haidvogel (1986) somewhat more extensively than here.

The quadrature points in physical space are

$$\left.\begin{aligned} (x,y) &= (i,j)\,\frac{2\pi}{N_x}, \\ z &= (p+\tfrac{1}{2})\,\frac{\pi}{N_z}, \end{aligned}\right\} \tag{11}$$

where $1 \leqslant i,j \leqslant N_x$. The vertical eigenmodes satisfy

$$\left.\begin{aligned} &\frac{\mathrm{d}}{\mathrm{d}z}\left(N^{-2}(z)\,\frac{\mathrm{d}F}{\mathrm{d}z}\right) + \lambda^2 F = 0, \\ &\frac{\mathrm{d}F}{\mathrm{d}z} = 0 \quad \text{at} \quad z = 0, \pi, \end{aligned}\right\} \tag{12}$$

and, for the special case $N(z)$ a constant,

$$\left.\begin{aligned} \lambda_p &= pA, \\ F_0(z) &= 1, \\ F_p(z) &= \surd 2 \cos pz, \quad p \geqslant 1, \end{aligned}\right\} \tag{13}$$

where $A = 1/N$ is the inverse first internal deformation radius. The vertical wavenumber may be thought of as either p or λ_p, although the latter is the one for which symmetry with $\boldsymbol{k}$ might be expected.

Initial conditions are chosen as a random realization of a moderately broadband horizontally isotropic energy spectrum:

$$\tau_p(k) = \frac{\mu^{\alpha_1}}{\left(\mu + \dfrac{\alpha_2}{\alpha_1}\mu_0\right)^{\alpha_1+\alpha_2}} \frac{1}{1+\left(\dfrac{\phi-\phi_0}{\delta\phi}\right)^{\alpha_3}} \tag{14}$$

for positive α_1, α_2, α_3, and $\delta\phi$. Here $k = |\boldsymbol{k}|$, and (μ, ϕ) is a polar representation of (k, λ),

$$\mu = (k^2 + \lambda_p^2)^{\frac{1}{2}}, \quad \phi = \tan^{-1}\left(\frac{\lambda_p}{k}\right). \tag{15}$$

The spectrum peak in (14) occurs at (μ_0, ϕ_0). The initial stream function transform is determined from

$$\hat{\psi}_p(\boldsymbol{k}, 0) = \Psi_0\, \mathrm{e}^{\mathrm{i}2\pi\gamma_p(\mathbf{k})}\, \tau_p(k)^{\frac{1}{2}} \mu^{-1} k^{-\frac{1}{2}}, \tag{16}$$

where $\gamma_p(\boldsymbol{k})$ is a random variable, uniformly distributed over $[0, 1]$, and the amplitude Ψ_0 is such that

$$T(0) = \tfrac{1}{2} \sum_{\boldsymbol{k},\, p} \mu^2 |\hat{\psi}_p(\boldsymbol{k}, 0)|^2 = 1. \tag{17}$$

4. Weak decay

Initial-value problems with finite viscosity exhibit a monotonic decay of T and V for the reasons discussed following (8). This behaviour is illustrated in figure 1 for a particular solution (A) which will serve as a benchmark for later parametric comparisons. (See table 1 for solution specifications.) The energy decreases by only a modest fraction over many time units, while the enstrophy decreases by several orders of magnitude during the same interval. Because of (17) a time unit would be a large-eddy circulation time if the energy were at the domain scale, and for energy primarily at smaller scales, as is true here initially, a circulation time is smaller than one. Because of inverse energy cascade and potential-enstrophy dissipation, a circulation time generally increases; for example, the particular definition $2\pi\{\zeta^2\}^{-\frac{1}{2}}$ has the values 0.2, 0.3, 0.8, and 1.8 at $t = 0$, 1, 5, and 30.

Since $\nu_\mathrm{v} = \epsilon = 0$ in solution A, the time derivatives of T and V are equal to minus the dissipation rates due to horizontal viscosity,

$$D_T = \nu_\mathrm{h} \sum_{\boldsymbol{k},\, p} k^6 |\hat{\psi}_p(\boldsymbol{k})|^2, \quad D_V = \nu_\mathrm{h} \sum k^6 \mu^2 |\hat{\psi}|^2, \tag{18}$$

and these quantities are plotted in figure 2. Energy dissipation reaches a peak value around $t = 0.15$, and the potential enstrophy dissipation peaks later at $t = 0.3$; these are on the order of initial eddy circulation times (see above). At late times, both D_T and D_V decline rapidly, approximately at a rate t^{-2}. At all times, $D_V \gg D_T$. Note the irregularity in D_V at late t; this is indicative of intermittency in the turbulent cascade process (transfer of potential enstrophy from larger scales to smaller), which is probably caused by the dominance of coherent vortices (§8).

Altogether this behaviour is qualitatively in conformity with the proposition, familiar from two-dimensional turbulence, that the energy dissipation rate decreases much more rapidly than the enstrophy dissipation rate as the Reynolds number increases towards infinity. Batchelor's (1969) energy-conserving similarity solution for two-dimensional turbulence embodies this proposition, and the $V(t)$ decline in figure 1, at a rate somewhat faster than t^{-1}, is even slower than the t^{-2} rate in the similarity solution. (In our solutions the exponent in the power-law dependence of

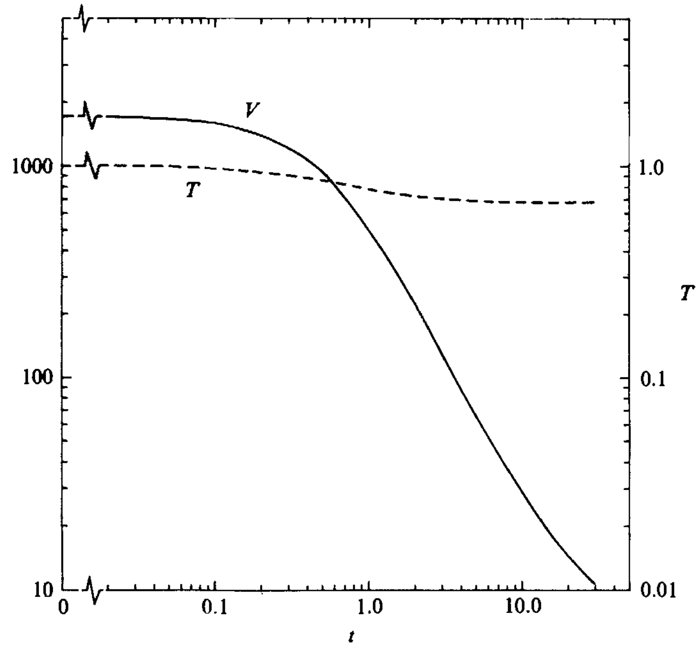

FIGURE 1. T and V for solution A; see (7) for definitions and table 1 for parameter specifications.

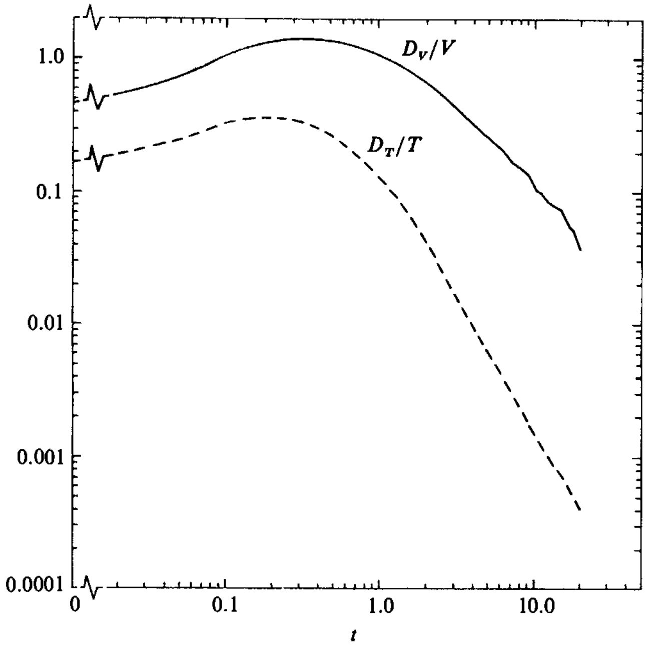

FIGURE 2. Dissipation rates for solution A; see (18) for definitions.

Solution	Λ	ν_h	μ_0	ϕ_0	N_x	N_z	Misc.
A	2	8.5×10^{-8}	22.6	0.785	192	32	$\nu_v = \epsilon = \beta = 0$, $\alpha_1 = 6$, $\alpha_2 = 12$, $\alpha_3 = 2$, $\delta\phi = 0.0833$†
B	2	8.5×10^{-8}	67.9	0.785	192	32	
C	2	4.0×10^{-7}	22.6	0.785	128	24	
D	2	4.0×10^{-7}	11.3	0.785	128	24	
E	2	4.0×10^{-7}	2.8	0.785	128	24	
F	2	4.0×10^{-7}	22.6	1.326	128	24	
G	2	4.0×10^{-7}	16.0	0	128	24	
H	—	4.0×10^{-7}	(see misc. →)		128	1	$\hat{\psi}_0(\boldsymbol{k}, 0)$ from solution G, renormalized by (17)
I	2	4.0×10^{-7}	22.6	0.785	128	12	
J	2	4.0×10^{-7}	22.6	0.785	128	32	
K	2	3.2×10^{-8}	22.6	0.785	256	12	
L	2	3.2×10^{-8}	22.6	0.785	256	24	
M	2	4.0×10^{-7}	22.6	0.785	128	48	
N	2	4.0×10^{-7}	22.6	0.785	128	64	
O	2	4.0×10^{-7}	22.6	0.785	128	80	
P	1	4.0×10^{-7}	11.3	0.785	128	64	
Q	2	2.5×10^{-6}	22.6	0.785	64	24	
R	1	4.0×10^{-7}	11.3	0.785	128	64	$\nu_v = 4 \times 10^{-7}$
S	1	4.0×10^{-7}	11.3	0.785	128	64	$\nu_v = 24 \times 10^{-7}$
T	2	4.0×10^{-7}	22.6	0.785	128	32	$\{q^2\}_h(z) \propto \exp\left[-\left(\frac{z-\pi/2}{\pi/8}\right)^2\right]$ at $t = 0$
U	2	4.0×10^{-7}	22.6	0.785	128	32	$\epsilon = 0.05$
V	8	3.2×10^{-8}	66.0	1.326	256	24	
W	1	4.0×10^{-7}	22.6	0.785	128	48	
X	4	4.0×10^{-7}	22.6	0.785	128	12	
Y	4	4.0×10^{-7}	22.6	0.785	128	32	$\epsilon = 0.05$
Z	2	4.0×10^{-7}	22.6	0.785	128	24	$\beta = 8$
AA	2	3.2×10^{-8}	22.6	0.785	256	24	$\beta = 3$

† These values apply to all solutions except as remarked in this column.

TABLE 1. Solutions

$V(t)$ is at least a weak function of numerical resolution and frictional coefficients.) The slowness of V-decay for $t > 1$ is indicative of a decrease in the turbulent cascade rate, due both to the arrival of significant energy on the limiting scale of the domain (§5), and to the emergence of coherent vortices which, when well separated from each other, adjust to configurations of zero nonlinear transfer (§8).

5. Inverse cascade, three-dimensional isotropy, and equipartition

Inverse cascade, the transfer of energy primarily towards larger scales, is a robust property of two-dimensional turbulence. So also is the forward cascade of enstrophy. However, with finite horizontal viscosity, the enstrophy arriving at small scales is efficiently dissipated, so that the peak of the surviving enstrophy spectrum will eventually also shift towards larger scales.

These tendencies have also been shown to occur in the antecedent studies of geostrophic turbulence. Evidence for this in the present calculations is shown in

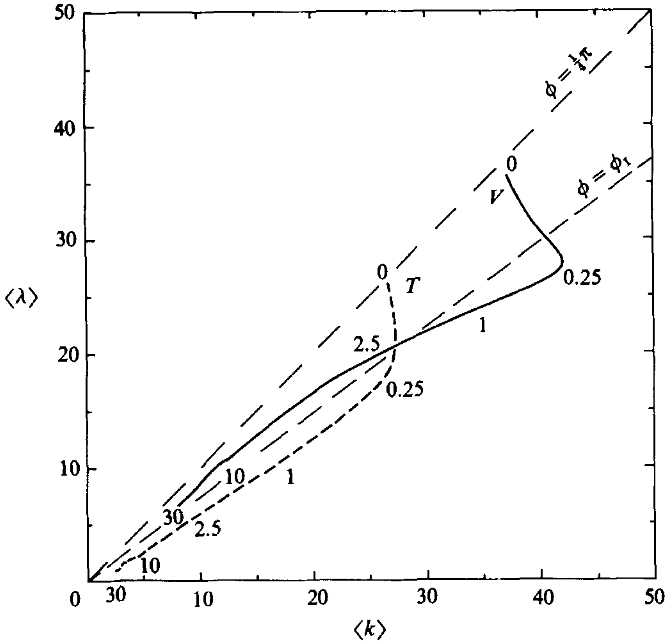

FIGURE 3. Centroid wavenumbers for T and V for solution A. Numerical labels indicate t-values along the wavenumber trajectories. Dashed lines are reference centroid angles.

figure 3. Centroid wavenumbers are defined as the weighted averages over all p and $\boldsymbol{k}$, where the weights are proportional to either the energy or enstrophy spectrum; for example,

$$\langle\mu\rangle_T = \frac{\sum\limits_{\boldsymbol{k},p} T(\boldsymbol{k},p)\,\mu}{\sum\limits_{\boldsymbol{k},p} T(\boldsymbol{k},p)} \tag{19}$$

is the centroid three-dimensional wavenumber for energy (note that $T(\boldsymbol{k},p) \equiv \frac{1}{2}\mu^2|\hat{\psi}_p(\boldsymbol{k},t)|^2$), and

$$\langle\mu\rangle_V = \frac{\sum\limits_{\boldsymbol{k},p} (\mu^2 T)\,\mu}{\sum\limits_{\boldsymbol{k},p} (\mu^2 T)} \tag{20}$$

is the centroid three-dimensional wavenumber for potential enstrophy. Analogous definitions obtain for $\langle k\rangle_T$, $\langle\lambda\rangle_T$, $\langle k\rangle_V$, and $\langle\lambda\rangle_V$.

For both T- and V-weights, the evolution is almost always towards smaller $\langle\mu\rangle$. An exception occurs for V at very early t while the dissipation rate is growing (figure 2), because transfer to larger μ has not yet been balanced by small-scale dissipation.

If the spectrum is three-dimensional isotropic (i.e. $T(\boldsymbol{k},p)$, a function of μ only), then

$$\left.\begin{aligned} \langle k\rangle_T &\propto \int_0^{\pi/2} \mathrm{d}\phi\,\cos^2\phi = \tfrac{1}{4}\pi, \\ \langle\lambda\rangle_T &\propto \int_0^{\pi/2} \mathrm{d}\phi\,\sin\phi\,\cos\phi = \tfrac{1}{2}. \end{aligned}\right\} \tag{21}$$

Here the discrete $(\boldsymbol{k}, p)$-sum is approximated by continuous wavenumber integrals, and the missing proportionality factors in (21), which depend upon the shape of T, are identical for $\langle k \rangle$ and $\langle \lambda \rangle$. The centroid wavenumber angle, i.e.

$$\langle \phi \rangle \equiv \tan^{-1}\left(\frac{\langle \lambda \rangle}{\langle k \rangle}\right), \tag{22}$$

with weights T or V, is at least a partial measure of the degree of isotropy between vertical and horizontal. From (21)–(22),

$$\begin{aligned} \langle \phi \rangle_T = \langle \phi \rangle_V = \phi_{\mathrm{I}} &\equiv \tan^{-1}\left(\frac{2}{\pi}\right) \\ &= 0.637 \end{aligned} \tag{23}$$

for a three-dimensional isotropic spectrum. (Note that $\langle \phi \rangle = \phi_{\mathrm{I}}$ is a necessary but not sufficient condition for isotropy.)

In figure 3 at early t, there are substantial shifts in $\langle \phi \rangle_V$ and $\langle \phi \rangle_T$ away from $\phi_0 = \frac{1}{4}\pi$ towards smaller ϕ. These tendencies, however, reverse or at least slow down after approximately a circulation time. Herring (1980) has shown that transfer rates in closure calculations of geostrophic turbulence are a decreasing function of ϕ, and the early tendency, $\langle \dot{\phi} \rangle < 0$, can be interpreted as a consequence of this. From initial conditions peaked about ϕ_0, there is an evolution towards three-dimensional isotropy, leading to a spreading of the spectrum in ϕ. Since the spreading rate is more rapid towards small ϕ than large, the centroid initially shifts towards small ϕ, but later reverses its tendency as the transfers to large ϕ catch up with those to small ϕ. A more extensive analysis of nonlinear transfer tendencies in geostrophic turbulence is presented in Herring & McWilliams (1988).

For the centroid trajectories in figure 3, the $\langle \phi \rangle$-values are listed in table 2. The small differences between ϕ_0 and the $\langle \phi \rangle$-values at $t = 0$ are due to discretization effects in evaluating (14)–(17). After the initial decrease in $\langle \phi \rangle_V$, the subsequent increase in monotonic for $t \in [0.3, 15.0]$, followed thereafter by a small decline. $\langle \phi \rangle_T$ is monotonically decreasing for all time, although the rate is slow after the first circulation time. The difference between T- and V-centroids is primarily a difference between large and intermediate spatial scales. Geostrophic turbulence is fundamentally anisotropic at the larger scales because $p = \lambda = 0$ (the barotropic mode) has a finite velocity while $\boldsymbol{k} = 0$ does not. In a bounded domain the anisotropy of wavenumber resolution is quantized, with $\lambda = 0, \Lambda, 2\Lambda, \ldots$ and $k = 1, 2, 3, \ldots$, and this anisotropy is of significance whenever there is a significant energy on the domain scale, which is almost always true here. (This anisotropy occurs with either a periodic vertical boundary condition or the present rigid-surface condition (6).) Thus figure 3 and table 2 indicate that the intermediate scales are not too far from isotropy, with $\phi_{\mathrm{I}} < \langle \phi \rangle_V < \frac{1}{4}\pi$, while the largest scales are anisotropic, biased towards larger vertical scales than horizontal ones, i.e. with $\langle \phi \rangle_T < \phi_{\mathrm{I}}$, because of the finite domain size. (The original proposal of isotropy in Charney 1971 was only for intermediate and smaller scales, albeit partly for geophysical reasons not relevant here.)

A more accurate and complete assessment of three-dimensional isotropy can be made by examining the horizontal-shell-integral form of the spectrum,

$$T_*(k, p) = \sum_{\substack{\boldsymbol{k} \ni \\ k - \frac{1}{2} < |\boldsymbol{k}| \leqslant k + \frac{1}{2}}} T(\boldsymbol{k}, p). \tag{24}$$

t	$\langle\phi\rangle_V$	$\langle\phi\rangle_T$
0	0.76	0.78
0.25	0.58	0.60
1.0	0.60	0.55
4.0	0.69	0.51
15.0	0.72	0.43
30.0	0.70	0.32

TABLE 2. Wavenumber centroid angles in solution A

When the solution is statistically independent of horizontal orientation, as it is here except for $\beta \neq 0$ (§12), then there is no loss of information in this summation of T. For three-dimensional isotropy, an ensemble average of $|\hat{\psi}_p(\boldsymbol{k})|$ is a function of μ only, hence $T(\boldsymbol{k},p) = \frac{1}{2}\mu^2|\hat{\psi}_p(\boldsymbol{k})|^2$ is as well. Since the shell integration in (24) yields a metric factor $k = \mu \cos\phi$, T_* is equal to $\cos\phi$ times a function of μ; figure 4 is a contour plot of $T_*(k,p)/\cos\phi$. The energy spectrum in figure 4(*a*) shows two adjacent peaks at small wavenumbers and an intermediate- and large-wavenumber regime where equal-energy contours are nearly parallel to lines of constant μ, and thus nearly three-dimensionally isotropic. However, an examination of departures from the isotropic component of the spectrum (figure 4*b*) shows that there is a prevalent pattern of greater energy at large ϕ for μ-values greater than the spectrum peaks; this is the cause of $\langle\phi\rangle_V > \phi_1$ in figure 3 and table 2. On the other hand the zone containing the spectrum peaks mostly has small ϕ values due to the finite domain size, and this is the reason for $\langle\phi\rangle_T < \phi_1$.

Again the relative slowness of nonlinear transfer at large ϕ (Herring 1980) can be invoked to explain the intermediate-scale anisotropy. In an approximately isotropic spectrum, the largest transfers will be to smaller and larger μ, with the effect of depleting the energy at intermediate μ. A slower depletion rate at large ϕ will yield larger energy values there, and thus lead to anisotropy as seen in figure 4(*b*).

The degree of departure from isotropy is influenced by the numerical resolution and anisotropy of the dissipation (which is totally horizontal in figure 4), but there is only weak influence from initial conditions; see §§6 and 7 below. Hua & Haidvogel (1986) also presented evidence for approximate isotropy from numerical solutions with lower and more anisotropic resolution.

For a three-dimensional isotropic solution, one can derive the energy and potential enstrophy component ratios

$$\frac{\frac{1}{2}\left\{\frac{1}{N^2}\left(\frac{\partial\psi}{\partial z}\right)^2\right\}}{\frac{1}{2}\{u^2+v^2\}} = \frac{1}{2}, \quad \frac{\{\eta^2\}}{\{\zeta^2\}} = \frac{3}{8}, \tag{25}$$

using a continuous approximation to the discrete grid in $\boldsymbol{k}$ and p. The first of these relations is referred to as energy equipartition. In our solutions, both ratios have an initial value of approximately 1.0 when $\phi_0 = \frac{1}{4}\pi$ in the non-isotropic formulae (14) and (16). Both ratios decrease rapidly during the first few circulation times; thereafter the energy ratio slowly decreases, while the potential-enstrophy ratio varies non-monotonically and only slightly. At intermediate times, the energy ratio is less than the isotropic value above and the enstrophy ratio is greater; for example,

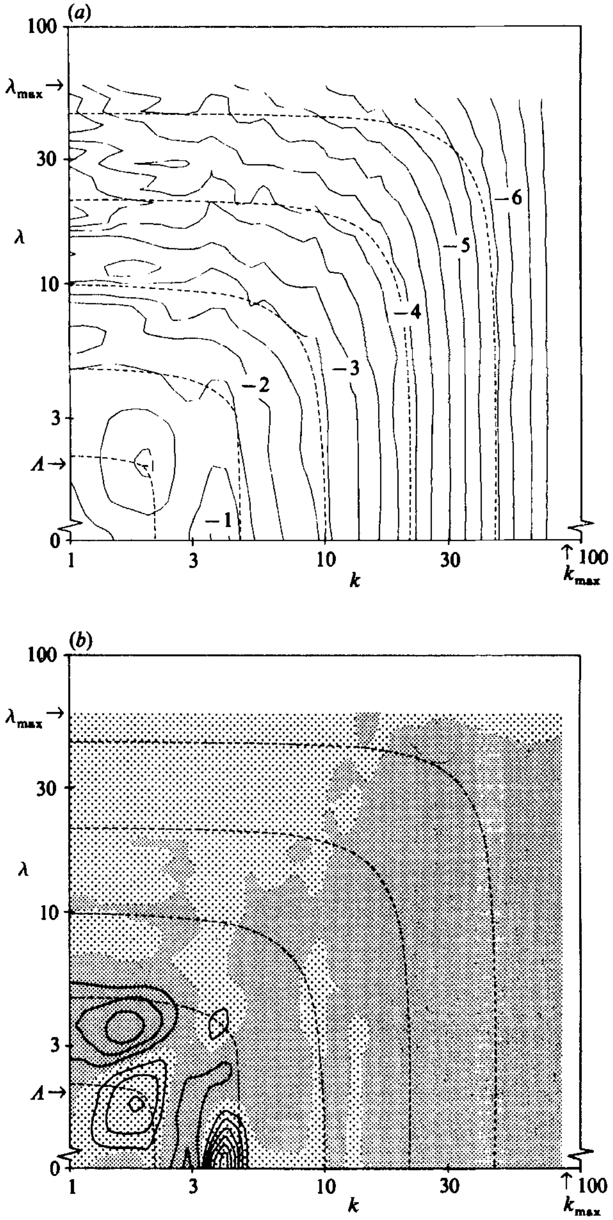

FIGURE 4. $T_*(k, \lambda)/\cos\phi$ from (24) for solution A, averaged over $6 \leqslant t \leqslant 8$. Dashed lines are curves of constant μ. (*a*) $\log_{10}\{T_*/\cos\phi\}$, with a contour interval of 0.33. (*b*) $T_*/\cos\phi$ minus its ϕ-average, with a contour interval of 0.01; light and dark stippling indicate positive and negative values, respectively.

in solution A at $t = 5$, the former has the value 0.34 (which is < 0.5 from (25)) and the latter has the value 0.53 (which is > 0.375 from (25)). The sense of the departures from isotropy is as seen in figures 3 and 4: the largest scales have relatively more kinetic energy and the intermediate and smallest scales have relatively more $\{\eta^2\}$ than in a wholly three-dimensional isotropic situation.

6. Numerical resolution and Reynolds number

The degree of three-dimensional isotropy is influenced significantly by the isotropy of the numerical resolution. The latter is determined from the largest available horizontal and vertical wavenumbers:

$$k_{\max} = (\tfrac{8}{9})^{\frac{1}{2}}\tfrac{1}{2}N_x, \quad \lambda_{\max} = \Lambda(N_z-1). \tag{26}$$

(The numerical factor $(\frac{8}{9})^{\frac{1}{2}}$ arises from the particular truncation rule yielding T- and V-conservation; see Orszag 1971.) In figure 5 solution isotropy is plotted as a function of the ratio of the resolution scales (26). In spite of the great variety of parameter values encompassed in these solutions, their results collapse to a considerable degree onto a monotonic dependence on the resolution ratio. Note that the degree of solution isotropy is approximately $\langle\phi\rangle_V = \frac{1}{4}\pi$ for isotropic numerical resolution, rather than ϕ_{I} from (23). The qualitative explanation for $\langle\phi\rangle_V > \phi_I$ is given in §5, but no quantitative explanation is yet available for this particular value of $\langle\phi\rangle_V$.

Other solution properties are also dependent on the numerical resolution. For each resolution the viscosity values have been chosen as small as possible, consistent with long-time smoothness of solutions and the avoidance of equipartition among all available modes; this is equivalent to making the grid Reynolds number slightly less than a critical value (Bennett & Haidvogel 1983). (The closeness to the critical value has been implemented only approximately, since *a posteriori* tuning is computationally expensive.) Thus for $\nu_{\mathrm{v}} = 0$, ν_{h} is chosen as a decreasing function of N_x (approximately N_x^{-4}) but independent of N_z and all other parameters as well; see table 1. Therefore, a bulk Reynolds number is a strongly increasing function of N_x. Among many possible definitions, the following is perhaps most relevant to the vorticity:

$$Re_{\mathrm{h}} = \frac{\{\zeta^2)^{\frac{1}{2}}}{\nu_{\mathrm{h}}\langle k\rangle_\zeta^4} = \frac{(\sum\limits_{\boldsymbol{k},\,p} k^4|\hat{\psi}|^2)^{\frac{9}{2}}}{\nu_{\mathrm{h}}(\sum\limits_{\boldsymbol{k},\,p} k^5|\hat{\psi}|^2)^4}, \tag{27a}$$

where $\langle k\rangle_\zeta$ is the centroid k for vorticity. Table 3 lists properties of representative solutions for a range of N_x between 64 and 256. The corresponding Re_{h} span a range of nearly two orders of magnitude. Re_{h} increases with time because the inverse cascade diminishes $\langle k\rangle_\zeta^4$ faster than dissipation diminishes $\{\zeta^2\}^{\frac{1}{2}}$, although this trend must eventually reverse at very large t. The relatively small initial values of Re_{h} are due to the broadband nature of the initial conditions. An alternative Reynolds number

$$Re_\lambda = \frac{\{u^2+v^2\}^{\frac{1}{2}}}{\nu_{\mathrm{h}}}L_\lambda^3 \tag{27b}$$

is based upon the Taylor microscale,

$$L_\lambda = \left[\frac{\{\zeta^2\}}{\{u^2+v^2\}}\right]^{\frac{1}{2}},$$

and it is more representative of the most energetic motions in the solution. Its values are also listed in table 3. They show the same trends as Re_{h} with t and N_x. Re_λ is always larger than Re_{h}, by as much as two orders of magnitude. Thus the solutions with N_x large are appropriately described as having large Re.

Other properties in table 3 also vary with N_x. The viscous decay rate for T

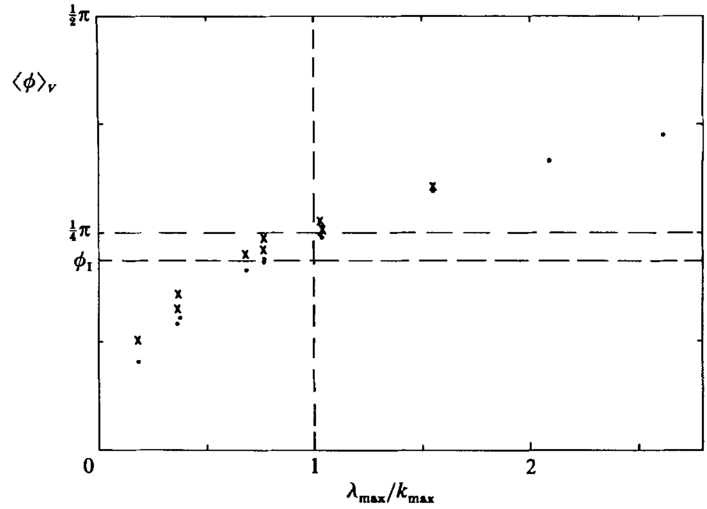

FIGURE 5. Isotropy of solution ($\langle\phi\rangle_V$) as a function of isotropy of numerical resolution; see (26) for definitions. Dots are for $t = 2$ and crosses are for $t = 10$. Solutions are (left to right) K, I, L, A, C, D, J, P, M, N, and O; all solutions have $\phi_0 = \frac{1}{4}\pi$, but μ_0, A, N_x, and N_z vary.

Solution	N_x	$Re_h(t = 0, 10)$	$Re_\lambda(t = 0, 10)$	$T(0) - T(10)$	$\frac{\langle\mu\rangle_T(10)}{\langle\mu\rangle_T(0)}$	$\frac{V_{p=0}}{V}(10)$	$Ku_\zeta(10)$
Q	64	29, 53	44, 555	0.88	0.27	0.09	3.7
C	128	49, 554	110, 1.8×10^4	0.55	0.13	0.19	11.2
L	256	397, 2160	1200, 2.0×10^5	0.18	0.13	0.20	31.7

TABLE 3. Horizontal resolution

decreases with increasing resolution. In any particular solution, the dissipation rates D_T/T and D_V/V are strongly varying with time (figure 2). For the solution sequence in table 3, D_T/T decreases approximately as N_x^{-2} (or approximately as Re_h^{-1}) for each t, whereas D_V/V does not show any strong or persistent dependence upon N_x. Thus the potential-enstrophy dissipation rate is not a strong function of Reynolds number in these solutions. The inverse cascade, measured both by the fractional change in $\langle\mu\rangle_T$ and by the fraction of the potential enstrophy transferred into the barotropic mode, proceeds farther. Finally, the vorticity field becomes increasingly spatially intermittent, as indicated by the large values of kurtosis,

$$Ku_\zeta = \frac{\{\zeta^4\}}{\{\zeta^2\}^2}. \tag{28}$$

This intermittency is due to the development of coherent vortices (§8).

Even though vertical resolution is quite important for three-dimensional isotropy (figure 5), N_z has less influence on the properties included in table 3 than does N_x. The greatest sensitivity is for N_z much smaller than an isotropic resolution value (e.g. solutions K and I), where T-decay is anomalously low and the barotropic fraction anomalously high; in contrast, there is little variation with larger N_z. An extreme of $N_z = 1$ (two-dimensional flow; e.g. solution H) also exhibits anomalously low T-decay compared with fully three-dimensional solutions.

Thus far, we have discussed solutions with horizontal friction only (i.e. $\nu_\mathrm{v} = 0$ in (8)). The converse ($\nu_\mathrm{h} = 0$) cannot be implemented without evolving towards modal equipartition on a circulation timescale, unless ν_v is so large that the evolution is only weakly nonlinear. However, for fixed ν_h, a sequence of solutions with increasing ν_v only slowly diverges from that with $\nu_\mathrm{v} = 0$. The principal effects of finite ν_v are to steepen the rate of decrease of $T(k,\lambda)$ with λ (and thereby to diminish centroid ϕ-values) and to increase total dissipation. For isotropic viscosity, $\nu_\mathrm{v} = \nu_\mathrm{h}$, the effects of vertical viscosity are small (e.g. comparing solutions P and R with $\nu_\mathrm{v} = 0$ and $= \nu_\mathrm{h}$, respectively): after an initial adjustment period on the order of a circulation time, the vertical dissipation rate for energy is less than one third the horizontal, and the total T-decay by $t = 5$ is only enhanced by about 5%. To get isotropic dissipation rates (where the energy dissipation rates associated with ν_v and ν_h are equal; i.e.

$$\nu_\mathrm{h}\{(\boldsymbol{\nabla}\zeta)^2\} = \nu_\mathrm{v}\left\{\left(\frac{\partial^2}{\partial z^2}\boldsymbol{\nabla}\psi\right)^2\right\}),$$

ν_v must be much larger than ν_h. This occurs when $\nu_\mathrm{v} = 6\nu_\mathrm{h}$ in solution S, and even then total T-decay is only enhanced by about one third over solution P. For two solutions with $A = 1$ and $\lambda_\mathrm{max}/k_\mathrm{max} = 1.04$ (i.e. solutions P and S),

$$\begin{aligned} \langle\phi\rangle_V\,(t = 10) &= 0.80 \quad \text{for} \quad \nu_\mathrm{v} = 0 \\ &= 0.68 \quad \text{for} \quad \nu_\mathrm{v} = 6\nu_\mathrm{h}, \end{aligned}$$

and even the latter value is larger than ϕ_I in (23), which indicates three-dimensional anisotropy in the same sense as in figure 4(*b*), in spite of vertical friction acting to diminish it.

Thus, within a substantial range, the anisotropy of the viscosity is not important to the qualitative properties of the solution. The relative inefficiency of vertical viscosity compared with horizontal may be interpreted as an inefficiency of potential-enstrophy transfer to replenish wavenumbers in the dissipation range with large polar angle ϕ. This is yet another consequence of the decrease of transfer rates with ϕ (Herring 1980).

7. Initial conditions

The spectrum properties described in §§4–6 occur for almost all initial conditions. This is illustrated in figure 6. Solutions with a wide variety of (μ_0, ϕ_0)-values have centroid wavenumbers that tend with time to converge towards small $\langle\mu\rangle_V$ and nearly isotropic $\langle\phi\rangle_V$. A weak memory of initial conditions is retained, however, since centroid positions at $t = 10$ have the same relative ordering as initially.

Of particular interest are the solutions with extreme initial conditions. For μ_0 sufficiently small (solution E), $\langle\mu\rangle_V$ initially increases although $\langle\mu\rangle_T$ continues to monotonically decrease. This is an example of initially nearly non-dissipative forward and inverse cascades, where, because of the large separation between the initial spectrum peak and dissipation scales, the energy transfer to a limited range of available large scales is accompanied for a finite interval by potential-enstrophy transfer to a much broader range of small scales at a rate faster than dissipation destroys it. For either extreme of ϕ_0 (solutions F and G), the initial evolution for several circulation times is such as to change $\langle\phi\rangle_V$ more than $\langle\mu\rangle_V$. These tendencies can be associated with instabilities of non-parallel (vortex-like) flows, which are characterized by Burger number B. For large B (or small $\langle\phi\rangle$), internal barotropic

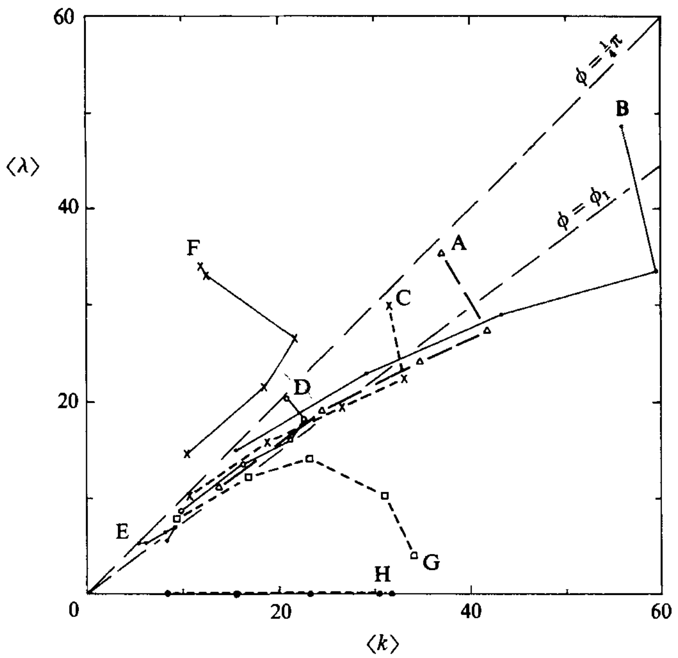

FIGURE 6. Centroid wavenumbers for V for solutions as labelled. Only the values at $t = 0$, 0.25, 1.0, 2.5, and 10.0 are plotted.

instability vertically fragments the flow structures (Gent & McWilliams 1986), while for small B (or large $\langle\phi\rangle$), baroclinic instability leads to horizontal fragmentation (Ikeda 1981; McWilliams, Gent & Norton 1986); in either case the fragmentation yields a less extreme Burger number and $\langle\phi\rangle$ for the flow. These early-time tendencies can also be interpreted as the consequence of three-dimensional isotropization, i.e. the spreading of the spectrum in ϕ. Note in particular the relative slowness of the initial spreading for large ϕ_0 (solution G), which is a consequence of slower nonlinear transfer rates for larger ϕ. These transfer tendencies are more extensively examined in Herring & McWilliams (1988).

Also in figure 6 is a comparison between the inverse cascades of two-dimensional and geostrophic turbulence. The two-dimensional solution H has initial conditions which are identical to the $p = 0$ mode in solution G, except for renormalization to conform to (17). It is remarkable that the $\langle k\rangle_V$ values match each other to better than 10% for all time (the same is true for T-centroids), in spite of the fact that the geostrophic solution is making a transition from nearly two-dimensional initial conditions towards three-dimensional isotropy.

Other solution properties also vary as a function of initial scale (table 4). As μ_0 increases, total dissipation increases since more energy resides within the dissipation range of scales. Also, for larger μ_0, the inverse cascade transfers energy a greater distance in μ but it never arrives at quite as small μ-values at late t (e.g. the solution is less barotropic). Finally, the vorticity intermittency (i.e. Ku_ζ) is greatest when the initial conditions are at intermediate scales, because this yields the most favourable combination of large inverse cascade rate and weak energy decay rate.

Solution	μ_0	N_x	$T(0)-T(10)$	$\dfrac{\langle\mu\rangle_T(10)}{\langle\mu\rangle_T(0)}$	$\dfrac{V_{p=0}}{V}(10)$	$Ku_\zeta(10)$
E	2.8	128	0.014	0.46	0.34	6.3
D	11.3	128	0.215	0.18	0.24	16.3
C	22.6	128	0.546	0.13	0.19	11.2
A	22.6	192	0.317	0.13	0.20	22.6
B	67.9	192	0.773	0.10	0.15	9.6

TABLE 4. Initial scale

8. Vortex emergence

As has been frequently alluded to above, isolated, long-lived, vortical flow structures spontaneously develop in geostrophic turbulence, as they also do in two-dimensional turbulence. These vortices have their simplest structure in the ζ-field: they essentially have ζ of a single sign, decaying monotonically in the horizontal coordinates away from a central extremum, with azimuthal symmetry about a vertical axis of finite extent (figure 9 (plate 1) and figure 10). This configuration is an exact, steady solution of (1) when $\mathscr{F} = \beta = 0$, although such single-vortex solutions are not superposable.

A robust statistical measure of vortex dominance is the kurtosis (28), which expresses the degree of spatial sparseness of the vortices, as well as the relative weakness of other flow features which are less sparse. Ku_ζ increases monotonically in time (figure 7), and reaches values vastly different from Gaussian. Note that the kurtosis does not begin to grow rapidly until after several circulation times, well after the time of maximum dissipation rate (figure 2); this reflects the dominance of vortices only after the inverse cascade is well begun. On the other hand, the emergence of vortices is visually recognizable in $\zeta(x, y)$-patterns (as in figure 9) even within the first circulation time ($t \lesssim 0.25$).

Kurtosis for q and η also grows with time to large values; for example, in solution A at $t = 15$, $Ku_q = 40$ and $Ku_\eta = 23$, while $Ku_\zeta = 31$. At the core of a vortex, η has an extremum of the same sign as ζ, but it has a larger horizontal scale of decay away from the core; these properties lead to q being more spatially intermittent than ζ, and η being less intermittent. Recall that the kurtosis for ζ, and thus for q and η as well, also increases monotonically with resolution and Reynolds number (table 3), and it is largest for initial conditions of intermediate scale (table 4). It is also remarkable that, in the previously cited comparison of two-dimensional and geostrophic solutions (H and G, respectively), there is no significant difference in $Ku_\zeta(t)$. There is little dependence of kurtosis on N_z and ϕ_0.

After vortex emergence, the probability functions for almost all flow quantities are highly non-Gaussian. This is illustrated in figure 8 not only for ζ, which has a large kurtosis, but also for velocity, which does not. Compared to a Gaussian distribution of equivalent variance, there is a high probability of occurrence for large-amplitude values, with a compensating low probability for intermediate (for vorticity) or low (for velocity, stream function, etc.) values. Low values are relatively common for vorticity because these are typical of the space between the well-separated vortices at late times.

A striking feature of these probability functions is their exponential form, i.e.

$$P(a) \propto \mathrm{e}^{-|a|},$$

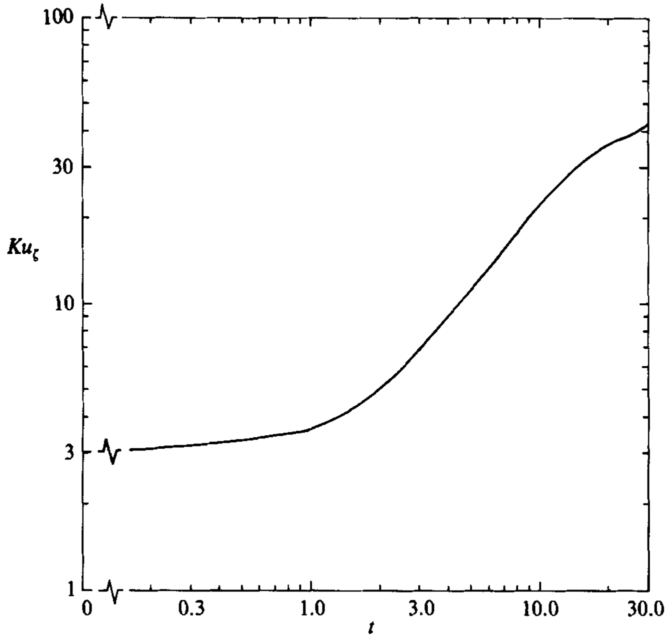

FIGURE 7. $Ku_\zeta(t)$ for solution A; see (28) for definition.

except for values of the amplitude a that are either very small or very large. The drop in $P(a)$ for large a is most likely due to under-sampling on the finite model grid, whereas the departure from exponential form near $a = 0$ is certainly not due to sampling error. Partial range exponential distributions have also been found experimentally for velocity in turbulent shear flow (Anselmet, Gagne & Hopfinger 1984) and for temperature in thermal convection (Heslot, Castaing & Libchaber 1987), and computationally for shear in stably stratified turbulence (Herring & Métais 1989), but a satisfactory explanation has not yet been found for this possibly quite general property of turbulent flows.

The vortices can have a great influence on the evolution of the statistical properties of geostrophic turbulence. At late times, when almost all of the vorticity is concentrated in vortices, then, since all other flow quantities can be calculated uniquely from ζ (§2), the dynamics of the flow evolution becomes nearly synonymous with the dynamics of the vortices. While it is beyond the scope of this paper to describe vortex processes in detail, a brief summary is given below to establish their conceptual relations with the statistical properties being examined here; further analyses will be reported in future (e.g. McWilliams 1988).

Vortices emerge from random initial conditions, in regions where the vorticity is predominately of one sign and larger than the local strain rate. This occurs through the processes of horizontal symmetrization (Melander, McWilliams & Zabusky 1987*a*) and vertical alignment (whereby ζ at adjacent vertical levels evolves towards a greater phase correlation). Subsequently such vortices resist deformations induced by straining due to neighbouring vorticity distributions, which is the central mechanism of forward cascade of potential enstrophy, and thereby diminish the cascade rate. (Isolated, symmetric, aligned vortices have zero nonlinear tendency; $J(\psi, q) = 0$.) For two-dimensional turbulence, the resistance of vortices to straining deformations has been demonstrated by Weiss (1981), McWilliams (1984), and

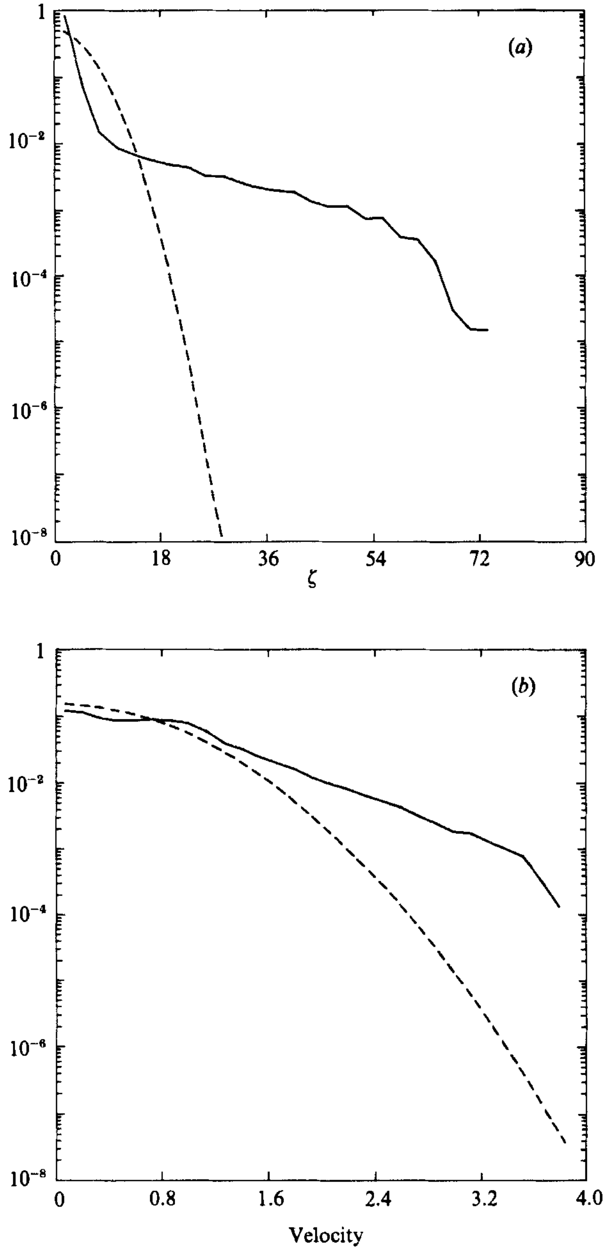

FIGURE 8. Normalized frequency distributions for (*a*) vorticity and (*b*) velocity components for all (x, y) quadrature points at $z = z_0$ (see (11)) from solution L at $t = 20$. Horizontally averaged kurtosis values are 34.3 and 3.4 respectively. Gaussian distributions with equivalent variance are also plotted (dotted lines).

Brachet *et al.* (1988), and the reduction in cascade rate has been demonstrated by comparing numerical solutions with vortices, and closure-theory solutions with limited intermittency (Herring & McWilliams 1985). This leads to relatively long vortex lifetimes, typically many circulation times, and a reduction in dissipation rate. When vortices are well separated from each other, they move under their

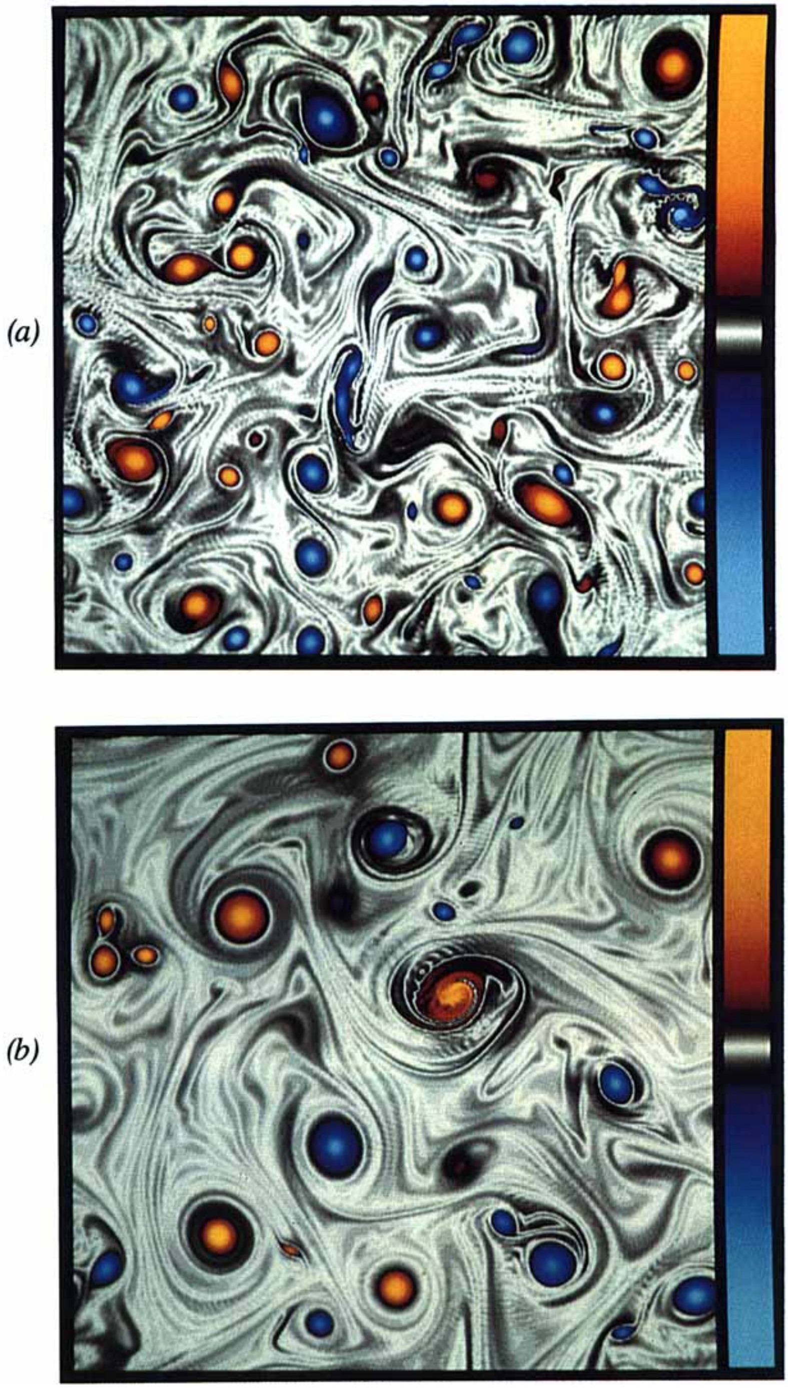

FIGURE 9. $\zeta(x,y,z = z_0)$ at (*a*) $t = 10$ and (*b*) $t = 20$ in solution L. The colour bar at the right has a linear variation with amplitude, from $\zeta = -90$ to $+90$, with the lightest grey centred at $\zeta = 0$.

mutual advective influence approximately as conservative point vortices (shown for two-dimensional turbulence by Benzi *et al.* 1988). However, when mutual advection causes close encounters between vortices, they undergo interactions which induce strong deformations from symmetry and alignment and which can be highly non-conservative. These interactions include dipole pairing of opposite-sign vortices, merger of like-sign vortices (Melander, Zabusky & McWilliams 1987*b*, 1988) whose cores are at approximately the same vertical level, attachment of like-sign vortices whose cores are separated vertically, and straining deformations which cause enhanced dissipation (even to the point of destruction) and may cause vertical fragmentation. In time many close vortex encounters occur, and the cumulative effect of these interactions is to have fewer surviving vortices, generally with larger size (both vertically and horizontally), with larger circulation, and with larger spatial separations (i.e. intermittency); collectively these tendencies represent a transfer of energy to larger wavenumbers (i.e. inverse cascade). Once vortices have emerged, dissipation is largely restricted to the non-conservative interactions during close encounters. As vortices become fewer and sparser, close encounters become rarer, and the potential-enstrophy dissipation rate becomes more intermittent (figure 2). Even at late times, most surviving vortices can be traced backwards in time to the initial conditions without ambiguity. Frictional decay of individual vortices is at a substantially slower rate than for the bulk measure $\{\zeta^2\}^{\frac{1}{2}}$, except during close encounters.

Vortex structure is illustrated in figures 9 and 10. In the horizontal cross-sections (figure 9, plate 1), one can see many of the features described above. Where vortices are well separated from each other, the typical shape is axisymmetric about a central extremum. For vortices in close proximity, substantial distortions from axisymmetry occur, including the expulsion of elongated filaments in which enhanced dissipation is occurring. Dipole pairing of opposite-sign vortices occurs (e.g. in the lower right quadrant and near the bottom to the left of centre in figure 9*a*). Merger of like-sign vortices is also occurring (e.g. near the top in figure 9*a*); following merger, symmetrization ensues (e.g. in the centre of figure 9*b*). With time there are fewer vortices, which typically are farther apart, larger, and less distorted from axisymmetry.

Surrounding the vortices in figure 9, ζ generally has a small amplitude, and its characteristic pattern consists of elongated filaments (signatures of the forward enstrophy cascade, induced by the external strain field from the vortices) and small-scale waves propagating on the horizontal shear field. Examples of the waves are the sinuous pattern between the opposite-sign vortex pair in the lower left of figure 9(*a*) (which probably arises as a parallel-shear-flow instability of the strong velocity between the nearby vortices), and the corrugated pattern surrounding the symmetrizing positive vortex in the centre of figure 9(*b*) (which is sufficiently close to the truncation scale in this solution that its details are of doubtful accuracy; in any event its amplitude is so slight as to have no important influence on larger-scale features).

In a three-dimensional perspective (figure 10), the vertical extent is seen to be highly variable, but it is almost always less than the domain height. In most instances the vortices are aligned vertically; exceptions occur during close interactions. Vortex Burger numbers ($B_* \equiv (\Delta z/\Lambda \Delta r)^2$, where Δz and Δr are vortex height and width) are typically larger than one. Partly this is a kinematic consequence of determining height and width from the ζ-field: for a three-dimensional isotropic energy spectrum, by calculations analogous to those in (21),

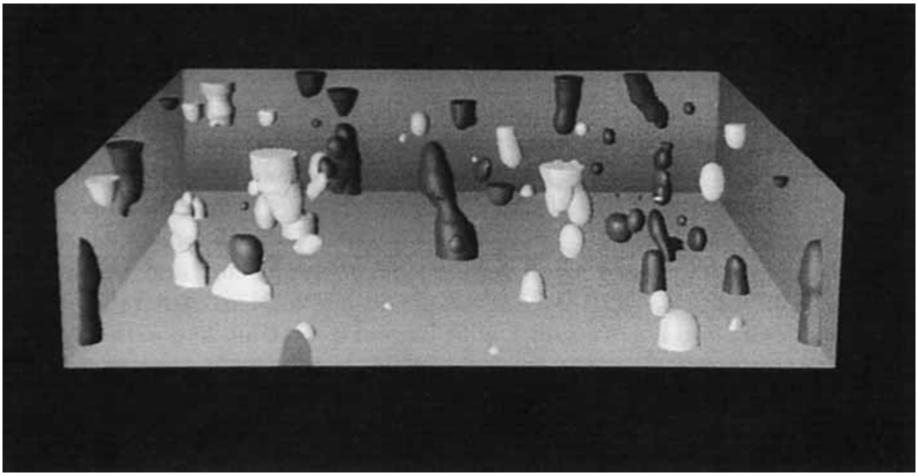

FIGURE 10. Isovorticity surfaces in solution A at $t = 20$. Vorticity values are $\zeta = +15$ (dark) and -15 (light). The viewing position is located at $(\pi, 6\pi, 3\pi)$ – recall the domain dimensions are $(2\pi, 2\pi, \pi)$ – and the light source is located at infinity along the major diagonal from the origin at (right, rear, bottom of the domain) through the appropriate domain boundary point at (left, front, top). The bottom and three of the side edges of the domain are included for orientation.

(23), and (25), a vorticity Burger number, $B_\zeta \equiv [\langle k \rangle_\zeta / \langle \lambda \rangle_\zeta]^2$, would have the value $(\frac{3}{4}\pi)^2 = 5.6$. However, for the strongest vortices in particular, B_* values are significantly larger than B_ζ. The probable explanation for this is that the surviving vortices have had to endure strong interactions during close encounters, and the relevant processes of symmetrization, merger, alignment, and attachment are more conservative of vortex structure for larger B_*. Consistency between the approximate three-dimensional isotropy of the spectrum and large B_* values requires that horizontal separations between vortex edges be typically larger than vertical ones, which they are. More vortices have their strongest extremum on the vertical boundaries than at any interior level, and this location bias is greater for the stronger vortices. Finally, there is a modest tendency for clumping of vertically separated, like-sign vortices, which often persists for quite long intervals with little non-conservative effect.

9. Vertical structure and inhomogeneity

The vertical boundary condition (6) imposes an inhomogeneity in the vertical. Even when the initial conditions are otherwise homogeneous, solutions spontaneously develop a degree of vertical inhomogeneity which increases with time. One manifestation of this, mentioned above, is the bias towards vortex cores being on the boundary (note (6) is conducive to ζ, η, and ψ having a vertical extremum there). An associated property is an edge enhancement of vorticity variance (figure 11), which increases monotonically with time. Vertical profiles of variance (figure 12) show a monotonic decay away from the edge for ζ and ψ, with the latter having a larger decay scale (associated with its spectrum peak at smaller μ); the decay scales vary inversely proportional to A (see also § 11). However, both η and q exhibit a sharp drop in variance between the quadrature points closest and next closest to the edge. This is a finite vertical representation of what appears to be a discontinuity in z; as N_z

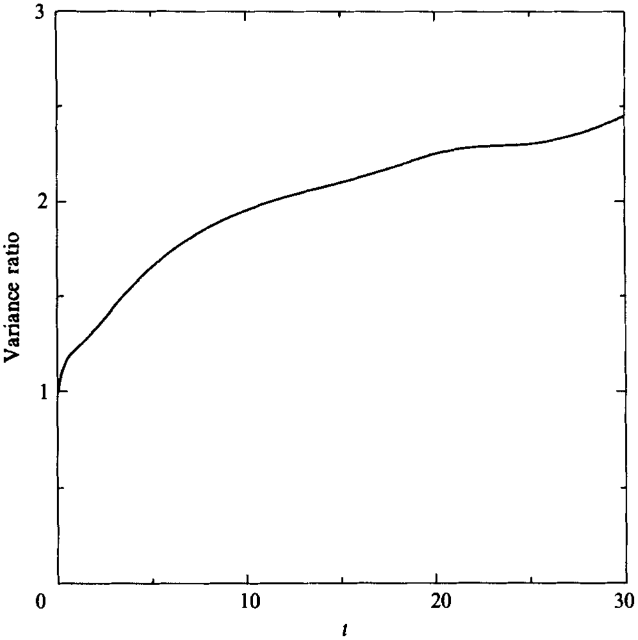

FIGURE 11. Evolution of the ratio of edge and centre ζ-variances (based upon a horizontal average) for solution A.

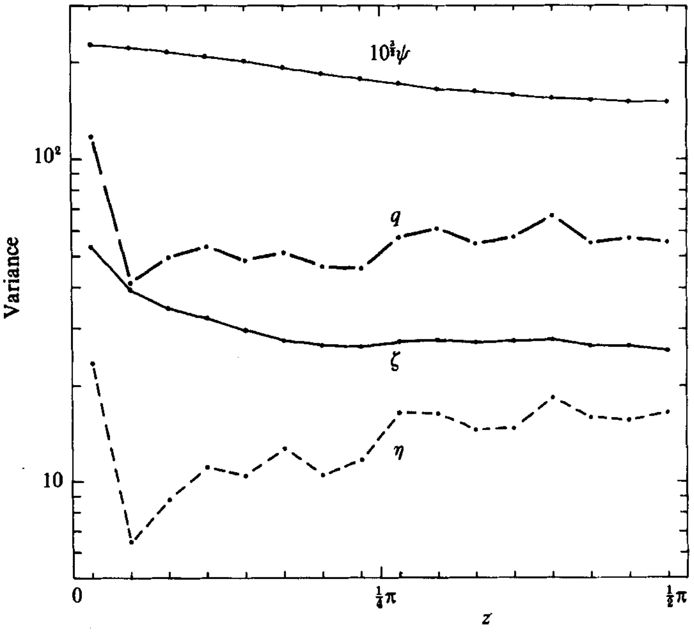

FIGURE 12. Vertical profiles of horizontal-average variance for solution A at $t = 10$. An average has been made using the symmetry between z and $\pi - z$.

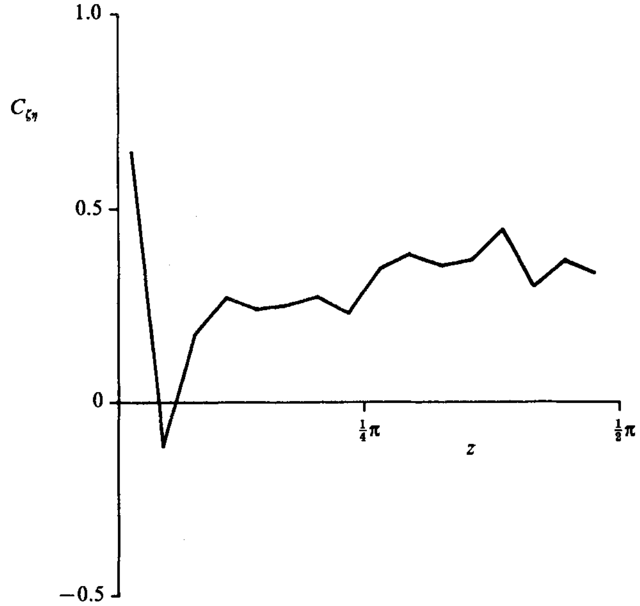

FIGURE 13. Vertical profile of correlation coefficient between ζ and η (solution A; $t = 10$).

increases (e.g. the sequence of solutions J, M, N, and O), its amplitude remains roughly constant while its width decreases as N_z^{-1}. (A modification occurs when the initial conditions are especially large scale in the vertical (e.g. solutions G and E): then the near-edge drop is spread over a larger interval in z.) There is a corresponding near-edge drop in the correlation between ζ and η (figure 13), which is particularly large at the edge, drops to approximately zero next to the edge, and rises to an intermediate positive value in the interior.

The vertical structure of second moments (figures 11–13) is at least partly a consequence of the vertical structure of vortices. At the core of a vortex with a shape as described in §8, ζ and η have extrema with the same sign, and thus combine to give q an enhanced extremum. At the edges, where vortex cores are particularly abundant and strong, both total variances and correlation are large. Near the edge, vortex cores are particularly rare because cores near the edge tend to migrate to the edge during close interactions (McWilliams 1988). Since η has a relatively short vertical correlation scale, the interior levels adjacent to the boundary levels have few η-extrema, and the variance of η and its correlation with ζ both have minima there. Further into the interior, the abundance of vortices is intermediate, and so are the second-moment values. However, the edge enhancement of ζ, etc., is not uniquely associated with vortices, since it also occurs in solution Z where β is large enough to destroy the vortices (§12).

Herring (1980) noted that there is nothing in the conservative quasi-geostrophic equations that enforces vertical homogeneity, in contrast to the Navier–Stokes equations in the absence of boundaries. A simple illustration of this is the conservation of horizontal-average enstrophy at each z in the absence of dissipation, so that any initial inhomogeneity in the q-variance profile will persist. This result also holds with vertical boundaries, so that the evolutionary inhomogeneity in figure 11 implies that dissipation has acted inhomogeneously in z (less dissipation, because of a reduced potential-enstrophy cascade, where vortices are most dominant).

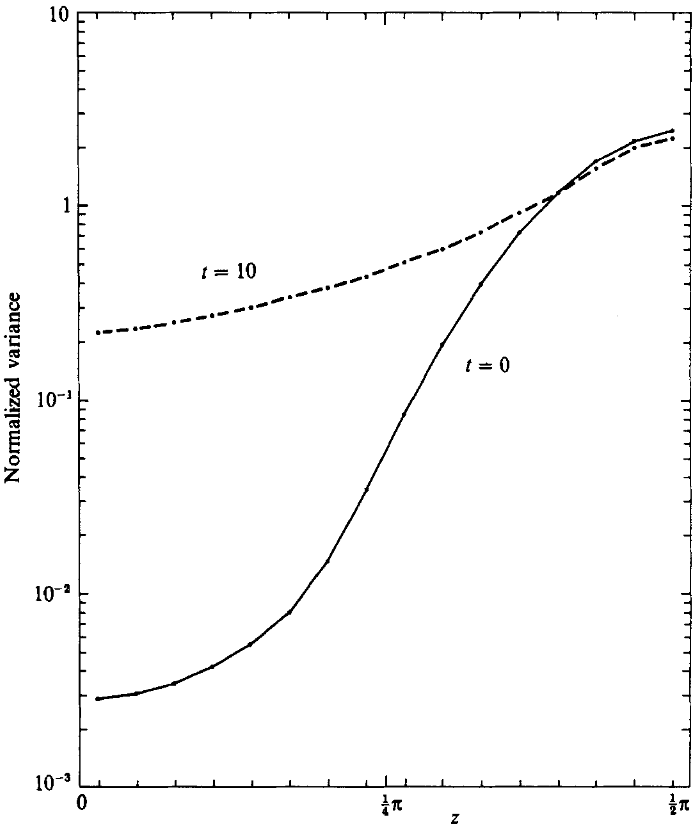

FIGURE 14. Vertical profiles of normalized r.m.s. vorticity (i.e. $[\{\zeta^2\}_h(z)/\{\zeta^2\}]^{\frac{1}{2}}$, where $\{\cdot\}_h$ is a horizontal average) at $t = 0$ and 10 in solution T.

When the initial conditions (14)–(17) are multiplied by a vertical envelope function to yield an inhomogeneous distribution, the sense of the inhomogeneity persists in time, although its degree tends to diminish. For the reason given above, changes in q-variance inhomogeneity can occur only through dissipative processes. Variances of other quantities are not so tightly constrained as q, but their behaviour is qualitatively similar. This is illustrated in figure 14 for an initial profile which is strongly centre concentrated, and which remains such but for weakly non-conservative homogenization. Other solution properties are qualitatively similar to those in the more homogeneous solutions discussed above, at least near the centre. In the vertical regions with small q-variance, however, the inverse cascade is inactive, vortices do not develop (Ku_ζ remains near the Gaussian value), and ζ and η have a strong negative correlation (so as to be minimally inhomogeneous subject to the constraint of the q-distribution; see (2)), in contrast to more active vortex-containing regions where the correlation is positive (figure 13). The absence of vortices where q is small is consistent with their emergence only through strong nonlinear interactions.

In geostrophic turbulence with a periodic vertical boundary condition, inhomogeneity could not develop from homogeneous initial conditions, but initial inhomogeneity would persist much as in figure 14.

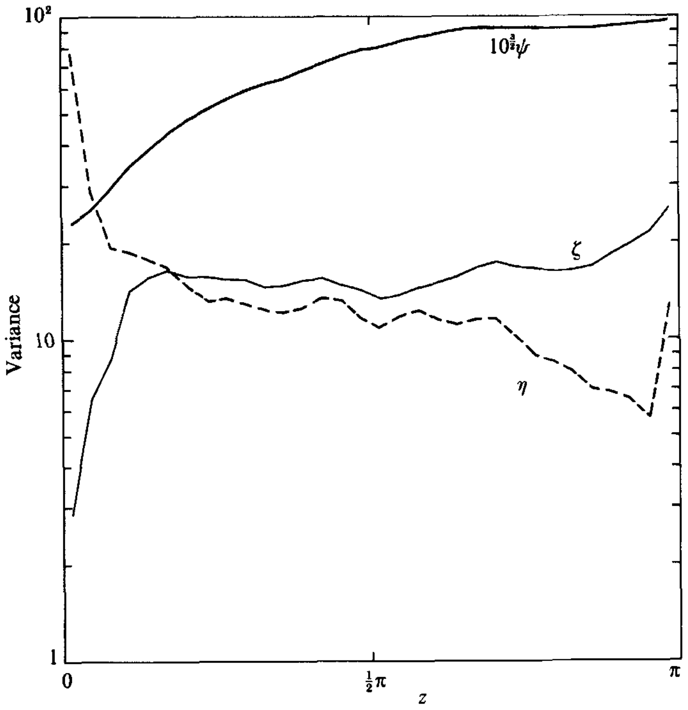

FIGURE 15. Vertical profiles of variance for solution U (with $\epsilon \neq 0$) at $t = 10$. The Ekman boundary layer is at $z = 0$.

10. Ekman friction

Another source of vertical inhomogeneity arises when ϵ is non-zero in (8), thus making the lower boundary a site of enhanced energy dissipation and a non-conservative torque (which is not sign definite in its effect on potential-enstrophy evolution). If vertical transfer processes were efficient, the resulting inhomogeneity might be slight; however, as might be anticipated from closure approximations (Herring 1980) and the results of the preceding sections, the transfer is inefficient and the inhomogeneity can be large.

Figure 15 shows vertical variance profiles from a solution with moderately small ϵ. ψ and ζ are greatly diminished in the vicinity of the Ekman boundary layer, while in contrast q and η are substantially enhanced, because strong vertical shears arise between the interior and the weak near-boundary flow. On the other hand, in the interior and near the upper, slippery boundary, these profiles are quite similar to those with $\epsilon = 0$ (cf. figure 12, disregarding a difference of overall variance amplitude due to different N_x and ν_{h}). This is further evidence of the ability of geostrophic turbulence to maintain vertical inhomogeneity.

A comparison is given in table 5 between two solutions that are the same except that one has Ekman friction. The differences between these solutions are plausibly the consequence of the effect illustrated in figure 15. Energy dissipation is necessarily enhanced with Ekman friction, but the size of the enhancement, here 12 %, need not be large since its effects are confined in z; once the flow is depleted near the boundary, its component of the dissipation rate due to ϵ becomes small. Net potential-enstrophy dissipation is even diminished by Ekman friction, probably because its effect is not

Solution	ϵ	$T(10)$	$V(10)$	$\dfrac{\langle\mu\rangle_T(10)}{\langle\mu\rangle_T(0)}$	$\langle\phi\rangle_V(10)$	$\dfrac{V_{p=0}}{V}(10)$
J	0	0.43	16.6	0.13	0.83	0.23
U	0.05	0.36	19.2	0.15	0.96	0.15

TABLE 5. Ekman friction

sign-definite for V. In addition, Ekman friction reduces flow near the boundary and thus decreases the largest available vertical scale; therefore, it causes an increase in the wavenumber centroid polar angle and a decrease in the barotropic fraction of T and V.

Finally, the kurtoses of ζ, η and q all drop to nearly Gaussian values in the vicinity of the Ekman boundary layer; i.e. coherent vortex structures do not occur there. In spite of this, the vortices are just as strong away from the Ekman layer as they are in solutions with only slippery vertical boundaries (e.g. the layer kurtoses are not significantly different between solutions J and U except near $z = 0$).

11. Stratification

If only the stratification strength is changed, the effect on the solution is quite large. A comparison of the first two solutions (L and V) in table 6 shows that decreasing the Brunt–Väisälä frequency N leads to much greater T- and V-decay, larger centroid modulus and angle, less potential enstrophy at large vertical scales, and less vorticity kurtosis. These solutions have the same N_x, N_z, and initial condition $\psi(x,y,z,0)$.

However, these changes are not fundamentally due to the change in stratification, but rather are indirect consequences of its change. The continuous problem posed in §2 is isomorphic under the following transformation:

$$(z, H, \nu_v, N) \rightarrow (\alpha^{-1}z, \alpha^{-1}H, \alpha^{-4}\nu_v, \alpha N), \tag{29}$$

where $H = \pi$ is the height of the domain and α is any positive constant. Thus, a given solution (L, say with $N = \frac{1}{2}$) can be reinterpreted as having a different N (e.g. $N = \frac{1}{8}$, the same as in solution V), in a different domain ($H = 4\pi$), in general with different vertical viscosity (except where $\nu_v = 0$ as here). The transformed vertical eigenmodes (12)–(13) have cosine argument ($p\pi z/H$) and the eigenvalues are $\lambda_p = p\pi/(HN)$; hence the stretched vertical wavenumber is unchanged by the transformation since the product HN is unchanged. Two important indirect consequences of the transformation (29) are

(i) The transformed initial conditions are unaltered in the (k, λ)-wavenumber space (i.e. μ_0 and ϕ_0 are the same in (14)), but the distribution in (k, p) can be quite different (whereas solutions L and V have identical (k, p) initial distributions);

(ii) the vertical spacing of quadrature points (11) changes by the factor α^{-1} in the transformed solution, while $\lambda_{\max}$ in (19) does not change (whereas solutions L and V have the same value for z_p and differ by a factor of 4 for $\lambda_{\max}$).

The discussions in §§6 and 7 show clearly that differences of numerical resolution and initial conditions can be quite important. To see how they dominate the comparison of solutions L and V, consider a different comparison set (solutions W, C, and X, also in table 6) where N_z is changed in direct proportion to N and the initial

Solution	$\Lambda = N^{-1}$	$\frac{\lambda_{\max}}{k_{\max}}$	$T(10)$	$V(10)$	$\langle\mu\rangle_V(10)$	$\langle\phi\rangle_V(10)$	$\sum_{p=0}^{P_*}\frac{V_p}{V}(10), P_*$	$Ku_\zeta(10)$
			$\psi(x,y,z,0)$ fixed					
L	2	0.38	0.82	71	20	0.55	0.59, 3	32
V	8	1.52	0.20	134	93	1.36	0.14, 0	12
			(μ_0, ϕ_0) fixed					
W	1	0.78	0.45	34	16	0.78	0.39, 3	10
C	2	0.76	0.45	33	17	0.77	0.38, 1	11
X	4	0.73	0.45	33	15	0.68	0.39, 0	10

TABLE 6. Stratification

conditions are for common (μ_0, ϕ_0). Such a specification reduces the indirect consequences of a change in stratification, although the solutions W, C, and X, still fail to be isomorphic under (29) through differences in domain height and stretched vertical wavenumber resolution. $\Delta\lambda = \lambda_{p+1} - \lambda_p$; any differences in their solution properties must be attributed to one of these influences. However, it is remarkable how few differences there are among solutions W, C, and X. Even the largest difference listed, for $\langle\phi\rangle_V$, can be rationalized as a discretization error due to the disproportionate influence the $p = 0$ mode has in sums over wavenumber in solution X with small N_z: the quantity in the eighth column in table 6 shows that, integrated over a common interval in λ, the amount of potential enstrophy in large vertical scales is nearly the same among these latter solutions.

The similarity of bulk properties for solutions W, C, and X demonstrates that vertical boundary effects are not of primary importance in these solutions, in spite of several demonstrable local consequences (see figures 11–13). The vertical decay scales for edge enhancement of vorticity variance and for Ekman frictional dissipation both vary approximately as N^{-1} (based upon comparisons of solutions W, C, and X (for $\epsilon = 0$) and U and Y (for $\epsilon \neq 0$)). Flow structures in physical space have quite different aspect ratios, as indeed they should from (29): the coherent vortices in solution W are much broader and shorter than those of solution X, for example. In spite of this, these vortices have a similar degree of dominance of the flow, as measured by vorticity kurtosis (table 6).

12. Rossby waves

When β is non-zero in (4), Rossby waves can occur with finite phase speed, and there is a competition between linear wave propagation and dispersion and nonlinear advection and spectrum transfer. In two-dimensional flow the major results of this competition are an arrest of the inverse cascade for $k \leqslant k_\beta$ (alternatively defined by different investigators as $\beta\{u^2+v^2\}^{-\frac{1}{4}}$ or $\beta\{\zeta^2\}^{-\frac{1}{2}}$, with a general weakening of nonlinear interactions in this range, and development of horizontal anisotropy at all k such that $u > v$ due to straining by the large-scale flow (Rhines 1975; Herring 1975; Holloway & Hendershott 1977). A particular aspect of the competition relates to coherent vortex emergence (McWilliams 1984). For an initial or forcing wavenumber k_0, vortices do not develop when $k_0 \leqslant k_\beta$, but do so when $k_0 > k_\beta$. If the vortices develop with a size close to k_β, they will be later destroyed by wave dispersion, with an initial growth of kurtosis (as in figure 7) followed by a collapse to a Gaussian value.

However, if the emergent vortex scale is much smaller ($k_0 \gg k_\beta$), vortices will persist in spite of dispersion and will limit the development of anisotropy. (Advective steepening can nearly cancel dispersive spreading in strongly nonlinear, isolated vortices with non-zero β (McWilliams & Flierl 1979).)

In geostrophic turbulence the competition with Rossby waves is very like that in two-dimension turbulence. To illustrate this, we define a horizontal anisotropy function $A(k,p,t)$ by

$$T(\boldsymbol{k},p,t) = T_0(k,p,t)\,[1-A(k,p,t)\cos 2\vartheta+\ldots] \tag{30}$$

or

$$A(k,p,t) = -\frac{2}{\pi}\int_{-\pi/2}^{\pi/2} \mathrm{d}\vartheta T(\boldsymbol{k},p,t)\cos 2\vartheta/T_0(k,p,t). \tag{31}$$

Here k and ϑ are the polar coordinates for the horizontal wavenumber vector $\boldsymbol{k}$, T is the total energy spectrum, T_0 is its azimuthal average (note that T_* from (24) is approximately equal to $\pi k T_0$), and the dots in (30) denote additional azimuthal components in T. Positive A indicates anisotropy such that $u > v$. (Note that A is unchanged by replacing T by either the stream function or the potential-enstrophy spectrum.)

Consider solution Z, which has $\beta = 8$ and $k_0 = 16$. If we use the definition $k_\beta = \beta^{\frac{1}{2}}(u^2+v^2)^{-\frac{1}{4}}$, then $\langle k\rangle_T/k_\beta = 8.7$ at $t=0$. During the early time interval $0 \leqslant t \leqslant 5$, inverse cascade occurs, vortices begin to develop, Ku_ζ grows, and the ratio $\langle k\rangle_T/k_\beta$ decreases from 8.7 to 1.8. In this phase, the spectrum-average anisotropy $A(t)$ remains small (figure 16*a*). After $t = 5$, however, Ku_ζ begins to decline towards 3, A grows, and $\langle k\rangle_T/k_\beta$ continues to decline towards approximately 1 ($A = 1.1$ and 0.7 at $t = 10$ and 20 respectively). After $t = 15$, A is nearly unity, which is as large as it can be, consistent with a non-negative T-spectrum in (23). Its distribution with k is qualitatively the same as in two-dimensional turbulence (compare figure 16*b* with figures 3–5 in Holloway & Hendershott 1977), and it is nearly independent of vertical wavenumber (figure 16*c*). Even though $\mathrm{J}(\psi, f)$ dominates $\mathrm{J}(\psi, q)$ in (1) only for the few smallest wavenumbers, anisotropy extends throughout the spectrum owing to advective straining of small-scale motions by anisotropic large-scale motions.

It is also remarkable that, in spite of the great differences in A and Ku_ζ values between solution Z and its counterpart with $\beta = 0$ (solution C), many other statistical measures are quite similar. For example, $T(t)$ and $V(t)$ never differ between the two solutions by more than a few percent over the interval $[0,20]$. However, there is a discernible arrest of the inverse cascade with β: centroid μ- and ϕ-values are larger in solution Z, especially for weighting functions emphasizing the larger scales (i.e. energy and stream-function spectra).

When $\langle k\rangle_T/k_\beta$ is initially somewhat larger (e.g. a value of 14.5 in solution AA), the evolution is strikingly different. $\langle k\rangle_T/k_\beta$ still decreases monotonically with time (the inverse cascade), but is does not approach 1 until quite late, after the coherent vortices have become well developed and are able to resist dispersive decay. As a result, the rate of growth of Ku_ζ diminishes, and Ku_ζ finally levels off at a large non-Gaussian value (figure 17). Compared to a solution with $\beta = 0$ (solution L), the $Ku_\zeta(t)$-curve does not begin to differ significantly until $\langle k\rangle_T/k_\beta$ drops below a value of about 3.0 around $t = 8$. In solution AA, the value of A is only 0.15, averaged over k, p, and $t \in [15,20]$. This degree of anisotropy is, of course, more than the $A = 0$ value with $\beta = 0$, but it is still much smaller than the $A \approx 1$ value with $\beta \neq 0$ but without persistent vortices.

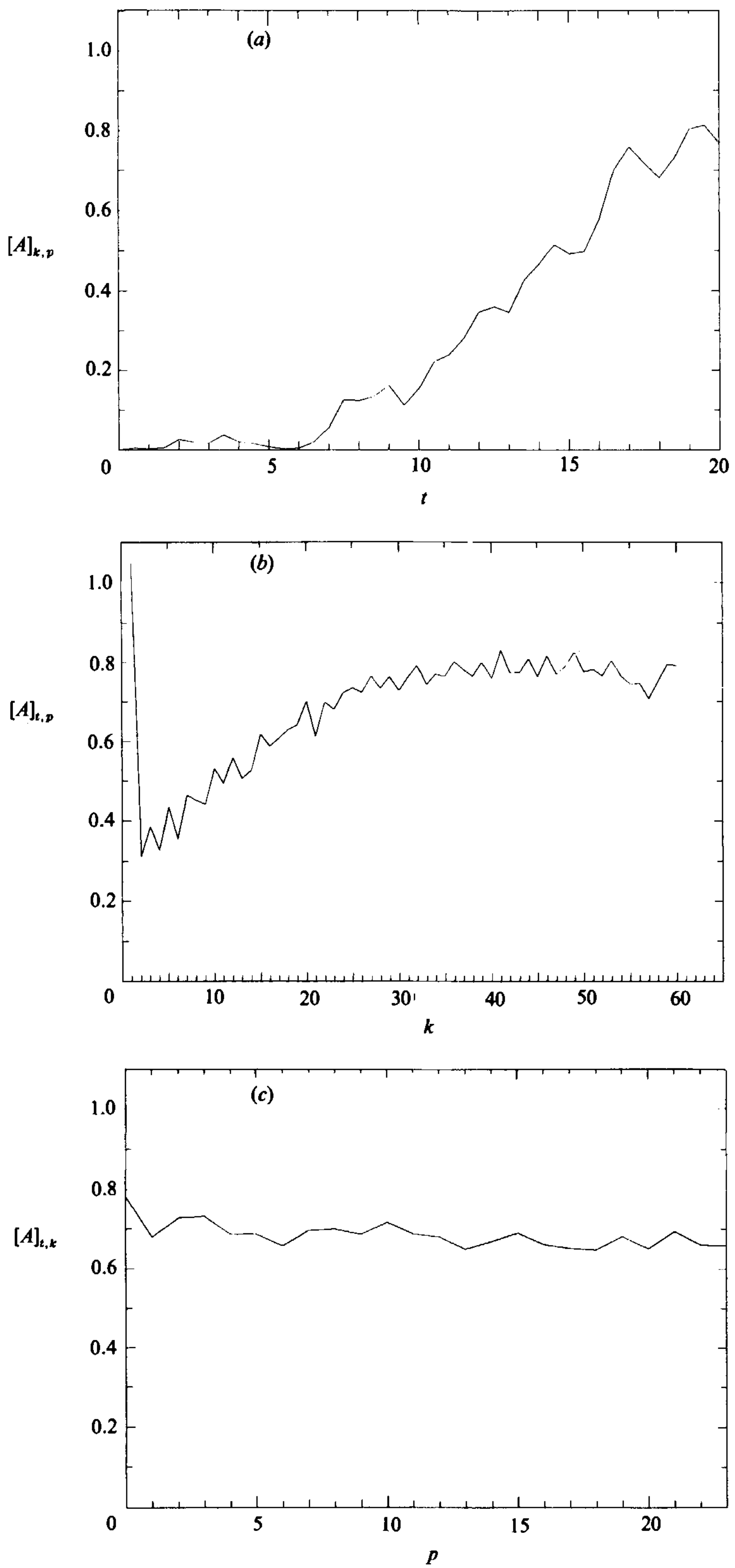

FIGURE 16. Partial averages of the horizontal anisotropy function $A(k, p, t)$ from (31) for solution Z. The arguments being averaged over are indicated by subscripts; the time average is over $t = 15$–20.

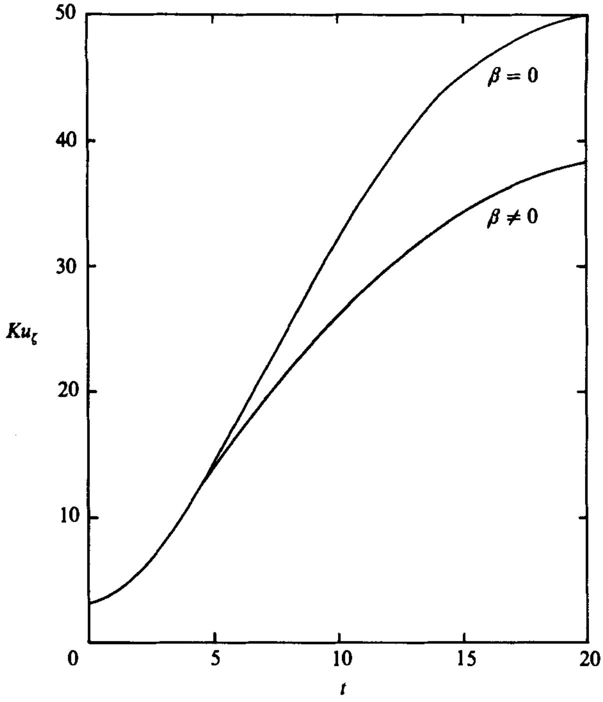

FIGURE 17. Ku_ζ for solutions L ($\beta = 0$) and AA ($\beta \neq 0$).

13. Physical and computational limits to inverse cascade

The preceding sections show that inverse cascade is a ubiquitous property of geostrophic turbulence when nonlinear advective processes dominate the flow evolution, and this occurs over broad but finite ranges of the physical and numerical parameters. Indicators of the inverse cascade are $\mathrm{d}\langle\mu\rangle_T/\mathrm{d}t$ substantially negative and $\mathrm{d}T/\mathrm{d}t$ only slightly negative. Here a brief summary is made of the known limits to the regime of inverse cascade.

For the initial-value problems as posed in §§2 and 3, with a time step small enough to prevent any computational instability or significant inaccuracy, inverse cascade will fail to occur for the following computational reasons:

(*a*) ν_h too small for a given N_x (evolution towards modal equipartition; see §6);

(*b*) N_x too small (computational inaccuracy for nonlinear transfer and excessive dissipation in order to avoid (*a*) above);

(*c*) certain combinations of $\lambda_{\max}/k_{\max}$ from (26), A from (13), and μ_0 and ϕ_0 from (14) too large (probably computational inaccuracy for weak nonlinear transfer);

(*d*) lack of conservation of both T and V in the numerical formulation of the Jacobian term in (1), which can exacerbate the preceding circumstances (Arakawa & Lamb 1977 found this to be true for two-dimensional flow).

Inverse cascade can also fail to occur for the following physical reasons:

(i) μ_0 in (14) too small (the small domain size prevents inverse cascade; see solution E in figure 6);

(ii) k_0 too large for a given N_x and ν_h (dissipation dominates nonlinear transfer);

(iii) any of ν_h, ν_v, or both ϵ and A in (8) and (13) too large (excessive dissipation);

(iv) β too large (excessive wave influence; see §12).

14. Summary and discussion

This paper reports on high-resolution, high-Reynolds-number numerical solutions of decaying geostrophic turbulence. A broad range of influences is examined, including anisotropy of viscosity and Ekman friction; anisotropy, scale content, and vertical inhomogeneity in initial conditions; strength of stratification and domain aspect ratio; gradient in Coriolis frequency (β); and numerical parameters.

These solutions exhibit inverse energy cascade, forward enstrophy cascade, three-dimensional isotropization, vertical inhomogeneity, substantial non-Gaussanity, and spontaneous development of coherent vortices.

The cascade rates are largest at early times, and they are later reduced because of enstrophy depletion, finite domain size, coherent vortices, and Rossby waves. After several large-eddy circulation times, the energy and enstrophy spectra are approximately three-dimensional isotropic; however, deviations occur at large scale because of the finite size of the domain, at intermediate scale because of a disequilibrium resulting from the relative slowness of nonlinear transfer for wavenumber vectors which are primarily vertical in orientation, and at small scale because of both the preceding influence and anisotropy of viscosity. Consequently, kinetic energy exceeds potential energy by more than the factor of two associated with equipartition, whereas the ratio of the stretching component of potential vorticity and the relative vorticity is larger than for a three-dimensional isotropic solution. The presence of solid, slippery, top and bottom boundaries enhances horizontal velocity and relative vorticity at the boundaries and diminishes stretching vorticity adjacent to them. However, when the boundaries exert a drag force (through an Ekman layer), the relative vorticity is locally diminished and stretching vorticity is enhanced. In general, vertical inhomogeneity is persistent in geostrophic turbulence.

Overall, it is striking how important the processes of two-dimensional turbulence are in geostrophic turbulence. The energy and enstrophy cascades certainly have strong similarities in the two systems. The development of horizontal anisotropy, cascade arrest, and competition between Rossby waves and vortices when β is non-zero are also quite similar (see figure 16*c* in particular). The emergence of coherent vortices and their intermittency and dominance of the flow evolution in the broad time interval between maximum enstrophy dissipation (around a large-eddy circulation time) and final viscous decay (at a time of order the inverse of Reynolds number) appear to be as important and fundamental in geostrophic turbulence as they are in two-dimensional turbulence. The limits to computable geostrophic turbulence (i.e. inverse cascade) listed in §13 are approximately coincident with limits to the emergence of coherent vortices. All of the two-dimensional vortex processes also occur in geostrophic flow, with important incremental effects due to vertical structure: finite vortex heights, vertical boundary effects and interactions between vortices centred at different levels (alignment, attachment, vertical straining deformation).

Finally, a cautionary remark should be made, similar to one made in Charney (1971). The largest scales of motions in the ocean and atmosphere, while mostly geostrophic in their momentum balance, differ in several important ways from the idealized geostrophic turbulence problem as posed here. There can be significant forcing of planetary-scale motions, important non-uniformity in the lower boundary or (for the ocean) side boundaries, spatial non-uniformity in stratification strength, and greater constraint due to the limited height of the fluid and greater influence of

β than in the cases examined here. The present problem, therefore, is more relevant to the smaller-scale geostrophic flows, under circumstances where the neglected larger-scale influences do not exert too great an influence on their evolution.

Support for this research was provided by the National Science Foundation through its contracts with the National Center for Atmospheric Research, Boeing Computing Services, and the Pittsburgh Supercomputing Center. I appreciate the contributions of Stuart Patterson, who provided multi-tasking and data management software; Nancy Norton, who developed and ran the computational model and analysis programs (starting from an earlier quasi-geostrophic model developed by Dale Haidvogel and Lien Hua); and Jackson Herring, who helped in the interpretation of spectrum shape. Joe Klemp, Matt McIrvin, and Michael Pierce assisted with the graphics (figures 9 and 10).

REFERENCES

ANSELMET, F., GAGNE, Y. & HOPFINGER, E. 1984 High-order velocity structure functions in turbulent shear flows. *J. Fluid Mech.* **140**, 63–89.

ARAKAWA, A. & LAMB, V. R. 1977 Computational design of the basic dynamical process of the UCLA general circulation model. *Methods in Computational Physics*, Vol. 17, pp. 173–265. Academic.

BATCHELOR, G. 1969 Computation of the energy spectrum in homogeneous, two-dimensional turbulence. *Phys. Fluids* **12**, 233–238.

BENNETT, A. & HAIDVOGEL, D. 1983 Low-resolution numerical simulation of decaying two-dimensional turbulence. *J. Atmos. Sci.* **40**, 738–748.

BENZI, R., PATARNELLO, S. & SANTANGELO, P. 1988 Self-similar coherent structures in two-dimensional decaying turbulence. *J. Phys.* A **21**, 1221–1238.

BRACHET, M., MENEGUZZI, M., POLITANO, H. & SULEM, P. 1988 The dynamics of freely decaying two-dimensional turbulence. *J. Fluid Mech.* **194**, 333–349.

CHARNEY, J. 1971 Geostrophic turbulence. *J. Atmos. Sci.* **28**, 1087–1095.

GENT, P. & MCWILLIAMS, J. 1986 The instability of barotropic circular vortices. *Geophys. Astrophys. Fluid Dyn.* **35**, 209–233.

HERRING, J. 1975 Theory of two-dimensional anisotropic turbulence. *J. Atmos. Sci.* **32**, 2254–2271.

HERRING, J. 1980 Statistical theory of quasigeostrophic turbulence. *J. Atmos. Sci.* **37**, 969–977.

HERRING, J. & MCWILLIAMS, J. 1985 Comparison of direct numerical simulation of two-dimensional turbulence with two-point closure: the effects of intermittency. *J. Fluid Mech.* **153**, 229–242.

HERRING, J. & MCWILLIAMS, J. 1988 Spectrum transfer in geostrophic turbulence. Preprint.

HERRING, J. & MÉTAIS, O. 1989 Numerical simulations of freely evolving turbulence in stably stratified fluids. *J. Fluid Mech.* (in press).

HESLOT, F., CASTAING, B. & LIBCHABER, A. 1987 Transitions to turbulence in helium gas. *Phys. Rev. A. Rapid Comm.* **36**, 5870–5873.

HOLLOWAY, G. 1986 Eddies, waves, circulation, and mixing: statistical geofluid mechanics. *Ann. Rev. Fluid Mech.* **18**, 91–147.

HOLLOWAY, G. & HENDERSHOTT, M. 1977 Stochastic closure for nonlinear Rossby waves. *J. Fluid Mech.* **82**, 747–765.

HUA, L. & HAIDVOGEL, D. 1986 Numerical simulations of the vertical structure of quasi-geostrophic turbulence. *J. Atmos. Sci.* **43**, 2923–2936.

IKEDA, M. 1981 Instability and splitting of mesoscale rings using a two-layer, quasi-geostrophic model on an *f*-plane. *J. Phys. Oceanogr.* **11**, 987–998.

MCWILLIAMS, J. 1983 On the relevance of two-dimensional turbulence to geophysical fluid motions. *J. Méc. Numéro Spécial*, pp. 83–97.

McWilliams, J. 1984 The emergence of isolated coherent vortices in turbulent flow. *J. Fluid Mech.* **146**, 21–43.

McWilliams, J. 1988 The vortices of geostrophic turbulence. Preprint.

McWilliams, J. & Flierl, G. 1979 On the evolution of isolated, nonlinear vortices. *J. Phys. Oceanogr.* **9**, 1155–1182.

McWilliams, J. C., Gent, P. R. & Norton, N. J. 1986 The evolution of balanced, low-mode vortices on the β-plane. *J. Phys. Oceanogr.* **16**, 838–855.

Melander, M., McWilliams, J. & Zabusky, N. 1987*a* Axisymmetrization and vorticity-gradient intensification of an isolated two-dimensional vortex through filamentation. *J. Fluid Mech.* **178**, 137–159.

Melander, M., Zabusky, N. & McWilliams, J. 1987*b* Asymmetric vortex merger in two dimensions: Which vortex is 'victorious'? *Phys. Fluids* **30**, 2610–2612.

Melander, M., Zabusky, N. & McWilliams, J. 1988 Symmetric vortex merger in two dimensions: causes and conditions. *J. Fluid Mech.* (in press).

Orszag, S. 1971 Numerical simulation of incompressible flows within simple boundaries. I. Galerkin (spectral) representations. *Stud. Appl. Maths.* **50**, 293–328.

Rhines, P. 1975 Waves and turbulence on the β-plane. *J. Fluid Mech.* **69**, 417–443.

Rhines, P. 1979 Geostrophic turbulence. *Ann. Rev. Fluid Mech.* **11**, 401–441.

Salmon, R. 1982 Geostrophic turbulence. In *Topics in Ocean Physics, Proc. Inst. Sch. Phys. Enrico Fermi, Varenna, Italy*, pp. 30–78.

Weiss, J. 1981 The dynamics of enstrophy transfer in two-dimensional hydrodynamics. *Rep.* LJI-TN-81-121. La Jolla Institute, La Jolla, California.